

Segment Anything Model for Medical Images?

Yuhao Huang*, Xin Yang*, Lian Liu, Han Zhou, Ao Chang, Xinrui Zhou, Rusi Chen, Junxuan Yu, Jiongquan Chen, Chaoyu Chen, Haozhe Chi, Xindi Hu, Deng-Ping Fan, Fajin Dong*, Dong Ni*

Abstract—The Segment Anything Model (SAM) is the first foundation model for general image segmentation. It designed a novel promotable segmentation task, ensuring zero-shot image segmentation using the pre-trained model via two main modes including automatic *everything* and manual *prompt* (e.g., points and boxes). SAM has achieved impressive results on various natural image segmentation tasks. However, medical image segmentation (MIS) is more challenging due to the complex modalities, fine anatomical structures, uncertain and complex object boundaries, and wide-range object scales. Meanwhile, zero-shot and efficient MIS can well reduce the annotation time and boost the development of medical image analysis. Hence, SAM seems to be a potential tool and its performance on large medical datasets should be further validated. We collected and sorted 52 open-source datasets, and built a large medical segmentation dataset with 16 modalities, 68 objects, and 553K slice. We conducted a comprehensive analysis of different SAM testing strategies on the so-called *COSMOS 553K* dataset. Extensive experiments validate that SAM performs better with manual hints like points and boxes for object perception in medical images, leading to better performance in *prompt* mode compared to *everything* mode. Additionally, SAM shows remarkable performance in some specific objects and modalities, but is imperfect or even totally fails in other situations. Finally, we analyze the influence of different factors (e.g., the Fourier-based boundary complexity and size of the segmented objects) on SAM’s segmentation performance. Extensive experiments validate that SAM’s zero-shot segmentation capability is not sufficient to ensure its direct application to the MIS.

Index Terms—Segment Anything Model, Medical Image Segmentation, Medical Object Perception

I. INTRODUCTION

The emergence of large language models such as ChatGPT¹ and GPT-4² has sparked a new era in natural language processing (NLP), characterized by their remarkable zero-shot and few-shot generalization abilities. This progress has inspired researchers to develop similarly large-scale foundational models

Yuhao Huang, Xin Yang, Lian Liu, Han Zhou, Ao Chang, Xinrui Zhou, Rusi Chen, Junxuan Yu, Jiongquan Chen, Chaoyu Chen and Dong Ni are with the National-Regional Key Technology Engineering Laboratory for Medical Ultrasound, School of Biomedical Engineering, Shenzhen University Medical School, Shenzhen University, Shenzhen, China, and also with the Medical UltraSound Image Computing (MUSIC) Lab, Shenzhen University, Shenzhen, China and the Marshall Laboratory of Biomedical Engineering, Shenzhen University, Shenzhen, China.

Haozhe Chi is with the Zhejiang University, Zhejiang, China. Xindi Hu is with the Shenzhen RayShape Medical Technology Co., Ltd, Shenzhen, China. Deng-Ping Fan is with the Computer Vision Lab (CVL), ETH Zurich, Zurich, Switzerland. Fajin Dong is with the Ultrasound Department, the Second Clinical Medical College, Jinan University and the First Affiliated Hospital, Southern University of Science and Technology, Shenzhen People’s Hospital, Shenzhen, China.

Yuhao Huang and Xin Yang contribute to this work equally.

Corresponding authors: Fajin Dong (dongfajin@szhospital.com), Dong Ni (email: nidong@szu.edu.cn)

¹<https://chat.openai.com>

²<https://openai.com/research/gpt-4>

for computer vision (CV). The first proposed foundation CV models have been primarily based on pre-training methods such as CLIP [1] and ALIGN [2]. CLIP can recognize and understand visual concepts and details, such as object shape, texture, and color, by associating them with their corresponding textual descriptions. This allows CLIP to perform a wide range of tasks, including image classification, object detection, and even visual question answering. ALIGN can generate natural language descriptions of image regions, providing more detailed and interpretable results than traditional image-captioning approaches. Then, DALL-E [3] was developed to generate images from textual descriptions. This model was trained on a large dataset of text-image pairs that could create a wide range of images, from photorealistic objects to surreal scenes that combine multiple concepts. However, these models have not been explicitly optimized for image segmentation, particularly medical image segmentation (MIS).

Recently, the *Segment Anything Model (SAM)* was proposed as an innovative foundational model for image segmentation [4]. SAM was based on the vision transformer (ViT) [5] model and trained on a large dataset with 11 million images containing 1 billion masks. The biggest highlight of SAM is its good zero-shot segmentation performance to unseen datasets and tasks. This process is driven by different prompts, e.g., points and boxes, for indicating the pixel-level semantics and region-level positions of the target objects. It has been proven to be highly versatile, and capable of addressing a wide range of segmentation tasks [4].

Based on the pre-trained models of SAM, several papers have further studied its performance in different zero-shot segmentation scenarios. We roughly divide them into two categories: 1) non-medical and 2) medical applications.

A. SAM in Non-medical Image Applications

Two studies focused on testing SAM’s performance under the *everything* mode in segmenting the camouflaged objects [6], [7]. The results show that its performance is poor in these scenes, e.g., camouflaged animals that are visually hidden in their natural surroundings. Besides, the authors found that SAM failed to detect concealed defects in industrial scenes [7]. Then, Ji et al. [8] explored three testing methods of the SAM (*points*, *boxes* and *everything*) for various applications. Specifically, their tasks cover natural images (salient/camouflaged/transparent object segmentation and shadow detection), agriculture (crop segmentation, and pest and leaf disease monitoring), manufacturing (anomaly and surface defect detection) and remote sensing (building and road extraction). They concluded that although SAM can achieve good performance in some scenarios, such as salient

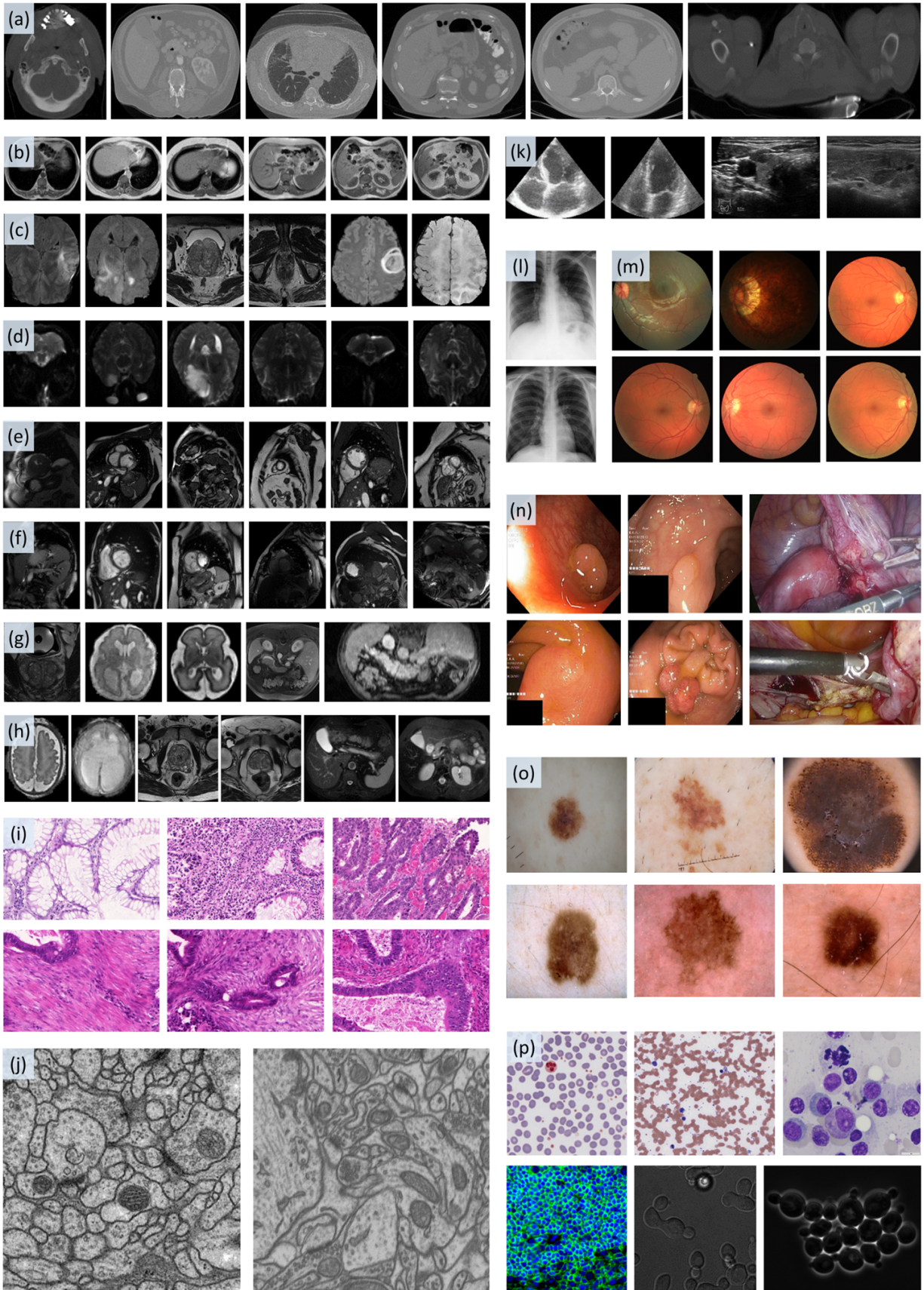


Fig. 1. Our *COSMOS 553K* dataset contains various modalities involving (a) CT, (b) T1-weighted MRI, (c) Multi-modal MRI, (d) Diffusion-weighted MRI, (e) CMR, (f) Cine-MRI, (g) MRI, (h) T2-weighted MRI, (i) Histopathology, (j) Electron Microscopy, (k) Ultrasound (US), (l) X-ray, (m) Fundus, (n) Colonoscopy, (o) Dermoscopy, and (p) Microscopy.

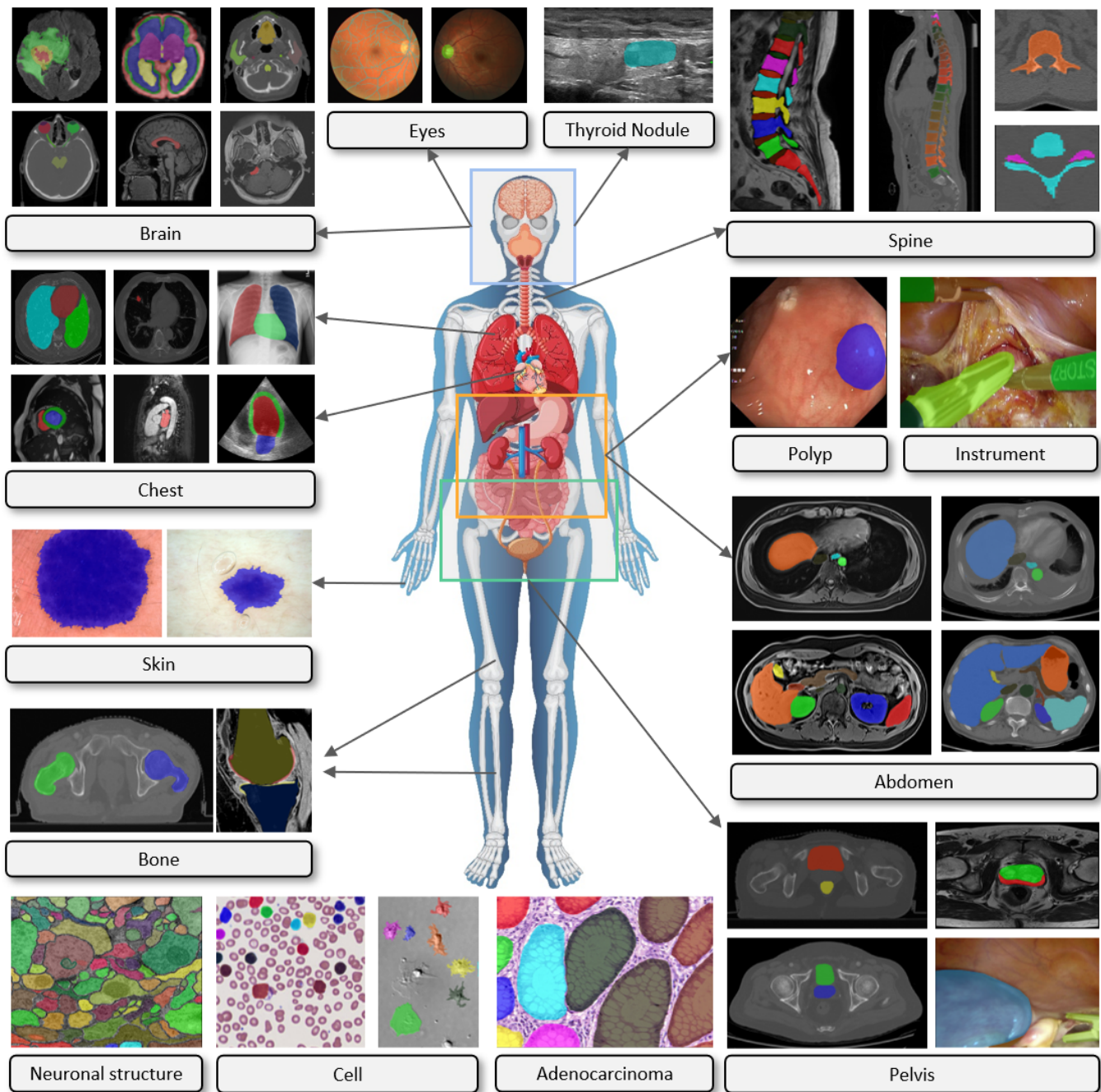


Fig. 2. Our *COSMOS 553K* dataset covers the majority of biomedical objects, for example, brain tumors, fundus vasculature, thyroid nodules, spine, lung, heart, abdominal organs and tumors, cell, polyp, and instrument, etc. *Image of human body by brgfx on Freepik [?]*.

object segmentation and agricultural analysis, it produces poor results in other applications. They also validated that human prompts can effectively refine the segmentation results compared to the automatic *everything* approach.

B. SAM in Medical Image Analysis

Ji et al. [7] assessed the SAM under the *everything* mode in segmenting the lesion regions in various anatomical structures (e.g., brain, lung, and liver) and modalities (computerized tomography (CT) and magnetic resonance imaging (MRI)).

The experimental results indicated that SAM is relatively proficient in segmenting organ regions with clear boundaries, but may struggle to accurately identify amorphous lesion regions. Another study then evaluated the performance of SAM in some healthcare subfields (optical disc and cup, polyp and skin lesion segmentation) using both automatic *everything* and two manual *prompt* (points and boxes) strategies [8]. The authors found that SAM requires substantial human prior knowledge (i.e., points) to obtain relatively accurate results on these tasks. Otherwise, SAM results in wrong segmentation

especially when no prompts are given. In the brain extraction task using MRI, Sovesh et al. [9] compared the SAM with the Brain Extraction Tool (BET) of the FMRIB Software Library. Quantitative results showed that the segmentation results of SAM were better than those of BET, demonstrating the potential of SAM for application in brain extraction tasks. Deng et al. [10] assessed the performance of SAM in digital pathology segmentation tasks, including tumor, non-tumor tissue and cell nuclei segmentation on whole-slide imaging. The results suggested that SAM delivers outstanding segmentation results for large connected objects. Nevertheless, it may not consistently achieve satisfactory performance for dense instance object segmentation, even with prompts of all the target boxes or 20 points per image. Zhou et al. [11] applied SAM to the polyp segmentation task using five benchmark datasets under the *everything* setting. The results show that although SAM can accurately segment the polyps in some cases, there is still a large gap between the SAM and the state-of-the-art methods. Besides, Liu et al. equipped the 3D Slicer software [12] with SAM to assist in the development, assessment and utilization of SAM on medical images [13].

Most recently, several studies tested the SAM on ≥ 10 public MIS datasets or tasks [14]–[17]. In [14], it was concluded that SAM’s zero-shot segmentation performance is (far) inferior to that of traditional deep learning-based methods. In [15], the authors evaluated SAM’s performance using different numbers of point prompts. They observed that as the number of points increases, the performance of SAM converges. They also noticed that SAM’s performance is 1) overall moderate, and 2) very unstable across different datasets and different cases. Ma et al. validated that the original SAM may fail on lots of medical datasets with the mean DICE score of 58.52% [16]. They then fine-tuned the SAM using medical images, and found that the proposed MedSAM achieved a 22.51% improvement on DICE compared with the SAM. Wu et al. adopted the *Adapter* technique to fine-tune the SAM and enhance its medical ability. Experiments validated that their proposed Medical SAM Adapter can outperform the state-of-the-art SOTA MIS methods (e.g., nnUnet [18]).

Although the above works investigated the performance of SAM in MIS, they had at least one of the following limitations:

- 1) Small datasets. Previous studies have only evaluated SAM’s performance in modalities, such as MRI, CT, and digital pathology, etc. Besides, they included a limit number of segmented objects. However, medical images contain multiple modalities and numerous of anatomical structures or other objects requiring segmentation. This has limited the comprehensive analysis in the field of MIS of the above studies [7]–[11].
- 2) Single SAM testing strategy. Most previous studies [7], [11], [15] evaluated SAM with limited or even only one type of testing mode/strategy. However, different medical objects often exhibit different characteristics and thus may have their own suitable modes for testing. The limited testing strategy may lead to inaccurate and incomplete analysis for SAM.
- 3) Lack of comprehensive and in-depth assessments. Some of the existing works [8] only assessed the SAM via

the visualization results provided by the online demo³. In addition, some studies focused only on limited metrics (e.g., DICE or IOU) to evaluate the performance of SAM [10]. Moreover, most of the studies did not investigate SAM’s perception of medical objects. In other words, the correlation of SAM’s segmentation performance and medical objects’ attributes have not been conducted carefully [14]–[16].

We think the analysis of medical object perception is very important. It can help the community better understand the factors that influence SAM segmentation performance (i.e., the ability to perceive medical objects), so as to better develop a new generation of general medical segmentation models.

In this report, we build a large medical image dataset named *COSMOS 553K* including 553K images with 16 different modalities (see Fig. 1) and 68 objects (e.g., anatomical structures, lesions, cells, tools, etc.) covering the entire body (see Fig. 2). This can help us to conduct a comprehensive analysis and evaluation of SAM’s performance on medical images. We then fully explore different testing strategies of SAM, and provide rich quantitative and qualitative experimental results to show SAM’s perception of medical objects. Finally, we deeply evaluate the correlation between SAM’s performance and the characteristics (e.g., complexity, contrast, and size) of the objects. We hope that this comprehensive report can provide the community with some insights into the future development of medical SAM.

II. DATASET

Medical images have various modalities such as CT, MRI, ultrasound (US), and X-ray, etc. There are large domain gaps between different modalities [19], and various modalities have their advantages in visualizing specific objects, including anatomical structures and lesions [13]. To fully evaluate the generalization performance of SAM in MIS, we collected 52 public datasets and standardized them to construct the large *COSMOS 553K* dataset. For the categorization system (e.g., modal categorization) of *COSMOS 553K*, we have referred to the official introduction of each public dataset and the recently-published study [20] (see Table I for more details). Fig. 1 and Fig. 2 illustrate various imaging modalities and most of the clinical segmentation objects covered in the dataset, respectively. We will describe the details of *COSMOS 553K* in the following two aspects, including image collection and preprocessing specification.

A. Dataset Collection

Medical images cover a wide range of object types, such as brain organs and tumors [28], [34], [41], [46], [65], lungs and hearts [22], [60], [63], [70], abdomen [21], [23], [56], [62], [65], [80], spine [64], [76], [77], cells [31], and polyps [37], [58], etc. Table I provides a detailed list of the collected MIS datasets and Fig. 3(a) gives the amount of each dataset after preprocessing. To be compatible with different modes in evaluating SAM, we have employed the following exclusion

³<https://segment-anything.com/demo>

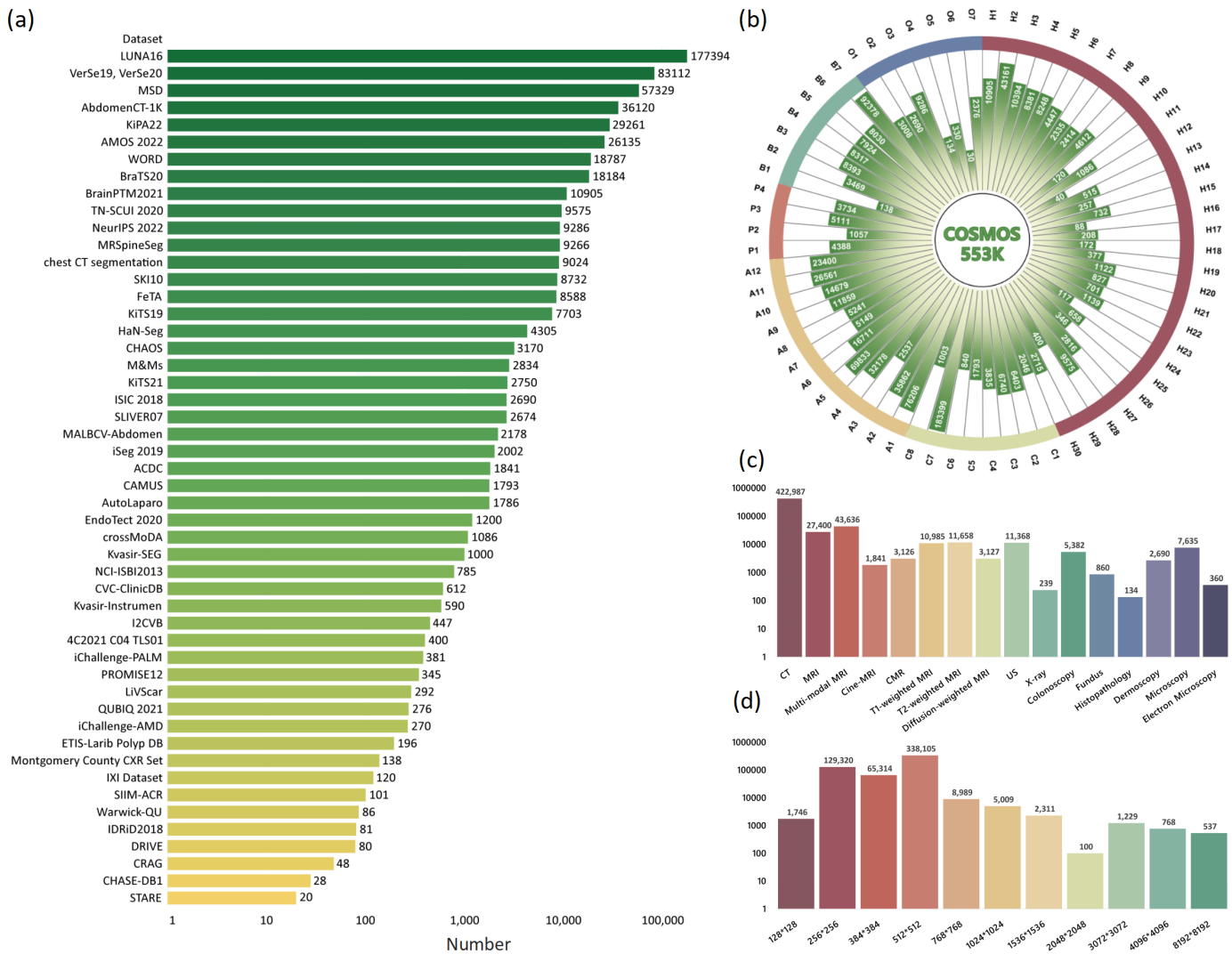


Fig. 3. Statistics of *COSMOS 553K* dataset. (a) Amount of datasets after preprocessing. (b) Histogram distribution of objects' quantity. (c) Amount of Modalities. (d) Histogram distribution of image resolutions. In (d), each bar represents an area interval distribution, e.g., $128 * 128$ represents the image area interval $(0, 128 * 128)$; $256 * 256$ represents the image area interval $(128 * 128, 256 * 256)$.

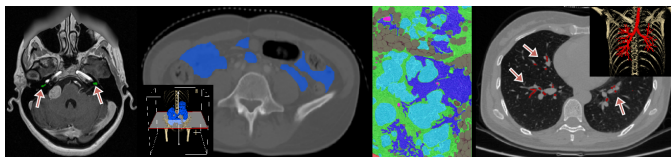


Fig. 4. Typical examples of meeting the exclusion criteria. From left to right: cochlea (criteria 1), intestine (criteria 2), histopathological breast cancer (criteria 3), and lung trachea trees (criteria 3). The corners (b) and (d) show the 3D rendering images obtained by *Pair* annotation software package [82].

criteria: 1) Exclude objects that are too small, such as the cochlea, shown in Fig. 4(a), and ureter. This is due to the difficulty of automatically generating points or boxes prompt on extremely small objects. 2) Exclude objects in the 3D volume where their overall target became significantly separated as the slice was sequentially extracted, such as the intestine (seen in Fig. 4(b)), mandible, and thyroid gland. We aim to avoid confusing the main object and generate unique boxes for each object. 3) Exclude objects with a relatively discrete overall

structure, such as histopathological images of breast cancer (see Fig. 4(c)), slices of lung trachea trees (see Fig. 4(d)), renal arteries, and veins. Most of these objects are dispersed into multiple items in a 2D slice and embedded in other objects, resulting in a failure to sensibly employ SAM's prompt mode on that objects to verify. According to the above criteria, *COSMOS 553K* finally included 68 objects. Their details and mapping abbreviations can be found in Table II. The histogram distributions of objects, modalities, and image resolutions are shown in Fig. 3.

B. Dataset Preprocessing Specification

Datasets often contain different labels, modalities, and data formats from one to another. To standardize the data across different datasets, we applied the following preprocessing steps for each collected public dataset.

For 3D volumetric data, the whole procedure can be summarized as follows: 1) Extract slices along the main viewing plane. In CT, it is usually a coronal plane, while in MRI,

TABLE I
DESCRIPTION OF THE COLLECTED DATASET. MALBCV-ABDOMEN IS AN ABBREVIATION FOR THE ABDOMEN DATASET OF MULTI-ATLAS LABELING BEYOND THE CRANIAL VAULT.

Dataset Name	Description	Image Modalities
AbdomenCT-1K [21]	Liver, kidney, spleen and pancreas	CT
ACDC [22]	Left and right ventricle and left ventricular myocardium	cine MRI
AMOS 2022 [23]	Abdominal multi-organ segmentation	CT, MRI
AutoLaparo [24]	Integrated dataset with multiple image-based perception tasks	Colonoscopy
BrainPTM 2021 [25]	white matter tracts	T1-weighted MRI, Diffusion-weighted MRI
BraTS20 [26]–[28]	Brain tumor	Multi-modal MRI
CAMUS [29]	Four-chamber and Apical two-chamber heart	US
CHAOS [30]	Livers, kidneys and spleens	CT, T1-weighted MRI, T2-weighted MRI
CHASE-DB1 [31]	Retinal vessel segmentation	Fundus
Chest CT Segmentation [32]	Lungs, heart and trachea	CT
CRAG [33]	Colorectal adenocarcinoma	Histopathological
crossMoDA [34]	Vestibular schwannoma	T1-weighted MRI
CVC-ClinicDB [35]	Polyp	Colonoscopy
DRIVE [36]	Retinal vessel segmentation	Fundus
EndoTect 2020 [37]	Polyp	Colonoscopy
EPFL-EM [38]	Mitochondria and synapses segmentation	Electron Microscopy
ETIS-Larib Polyp DB [39]	Polyp	Colonoscopy
FeTA [40]	Seven tissues of the infant brain	T2-weighted MRI
HaN-Seg [41]	Healthy organs-at-risk near the head and neck	CT
I2CVB [42]	Prostate	T2-weighted MRI
iChallenge-AMD [43]	Optic disc and fovea	Fundus
iChallenge-PALM [44]	Optic disc and lesions from pathological myopia patients	Fundus
IDRD 2018 [45]	Optic disc, fovea and lesion segmentation	Fundus
iSeg 2019 [46]	White matter, gray matter, and cerebrospinal fluid of infant brain	T1-weighted MRI, T2-weighted MRI
ISIC 2018 [47] [48] [49]	Melanoma of skin	Dermoscopy
IXI [50]	Callosum	T1-weighted MRI
KiPA22 [51] [52] [53] [54]	Kidney, tumor, renal vein and renal artery	CT
KiTS19 [55]	Kidneys and tumors	CT
KiTS21 [56]	Kidneys, cysts, tumors, ureters, arteries and veins	CT
Kvasir-Instrumen [57]	Gastrointestinal procedure instruments such as snares, balloons, etc.	Colonoscopy
Kvasir-SEG [58]	Gastrointestinal polyp	colonoscopy
LiVScar [59]	Infarct segmentation in the left ventricle	CMR
LUNA16 [60]	Lungs, heart and trachea	CT
M&Ms [61]	Left and right ventricle and left ventricular myocardium	CMR
MALBCV-Abdomen [62]	Abdominal multi-organ segmentation	CT
Montgomery County CXR Set [63]	Lung	X-ray
MRSpineSeg [64]	multi-class segmentation of vertebrae and intervertebral discs	MRI
MSD [65]	Large-scale collection of 10 Medical Segmentation Datasets	CT, MRI, Multi-modal MRI
NCI-ISBI 2013 [66]	Prostate (peripheral zone, central gland)	T2-weighted MRI
NeurIPS 2022 [67]	Cell segmentation	Microscopy
PROMISE12 [68]	Prostate	T2-weighted MRI
QUBIQ 2021 [69]	Kidney, prostate, brain growth, and brain tumor	CT, MRI, Multi-modal MRI
SIIM-ACR [70]	Pneumothorax segmentation	X-ray
SK110 [71]	Cartilage and bone segmentation from knee data	MRI
SLIVER07 [72]	Liver	CT
ssTEM [73]	Neuronal structures	Electron Microscopy
STARE [74]	Retinal vessel segmentation	Fundus
TN-SCUI 2020 [75]	Thyroid nodule	US
VerSe19, VerSe20 [76]–[78]	Spine or vertebral segmentation	CT
Warwick-QU [79]	Gland segmentation	Histopathological
WORD [80]	Abdominal multi-organ segmentation	CT
4C2021 C04 TLS01 [81]	Throat and hypopharynx cancer lesion area	CT

it may be a coronal plane, *e.g.*, prostate, brain tumor, or a sagittal plane, *e.g.*, spine and heart. 2) Retain slices with the sum of the pixel values of its labels greater than 50 for any 3D image and label volumes. This ensures that each slice has the corresponding correct label. 3) Normalize the extracted image and reset the pixel values of the mask according to the object category or location (*e.g.*, left and right). This is due to medical images may vary widely in the voxel or pixel values. Examples include MRI with an intensity range of (0, 800) and CT with an intensity range of (-2000, 2000), while other modalities may already be in the range of (0, 255) [20]. 4) Save images and labels in PNG format.

For 2D images, the preprocessing is as follows: 1) Retain images with the sum of the pixel values of their labels greater than 50. 2) Reset the pixel value of labels according to the object category or location ranging from 1 to 255. For NeurIPS

2022 dataset [67], due to the wide range of original label values (1-1600), we reconstruct each image and label into several sub-figures to ensure a uniform label range. 3) Convert the format of images and labels from BMP, JPG, TIF, etc. to PNG for achieving consistent data loading.

III. METHODOLOGY

A. Brief Introduction to SAM

SAM diverges from traditional segmentation frameworks by introducing a novel promptable segmentation *task*, which is supported by a flexible prompting-enabled *model* architecture and the vast and diverse sources of training *data*. A *data engine* was proposed to build a cyclical process that utilizes the model to facilitate data collection and subsequently leverages the newly collected data to enhance the model's performance.

TABLE II
OBJECT MAPPING. H: HEAD&NECK, C: CHEST, A: ABDOMEN, P: PELVIS, B: BONE, AND O: OTHERS.

Object	Mapping Abbreviation	Object	Mapping Abbreviation	Object	Mapping Abbreviation
Brain	H1	Pituitary Gland	H24	Esophagus	A9
Brain Tumor	H2	Larynx Supraglottic	H25	Stomach	A10
Cerebrospinal Fluid	H3	Larynx Glottis	H26	Aorta	A11
Brain Grey Matter	H4	Carotid Artery	H27	Inferior Vena Cava	A12
Brain White Matter	H5	Thyroid Nodules	H28	Prostate	P1
Brain Ventricles	H6	Throat Cancer	H29	Uterus	P2
Cerebellum	H7	Spinal Cord	H30	Bladder	P3
Brain Deep Grey Matter	H8	Heart	C1	Rectum	P4
Brainstem	H9	Left Ventricle	C2	Arytenoids	B1
Callosum	H10	Left Ventricular Myocardium	C3	Head of Femur	B2
Vestibular Schwannomas	H11	Right Ventricle	C4	Femur	B3
Eyeball	H12	Left Atrium	C5	Femur Cartilage	B4
Posterior Eyeball	H13	Left Atrium Appendage	C6	Tibia	B5
Anterior Eyeball	H14	Lung	C7	Tibia Cartilage	B6
Optic Disc	H15	Lung Tumor	C8	Vertebra	B7
Fundus Vasculature	H16	Liver	A1	Polyp	O1
Lacrimal Gland	H17	Pancreas	A2	Melanoma	O2
Optic Nerve	H18	Pancreatic Mass	A3	Neural Cell	O3
Cricopharyngeal	H19	Spleen	A4	Adenocarcinoma	O4
Parotid Gland	H20	Kidney	A5	Mitochondria	O5
Lips	H21	Kidney Tumor	A6	Neuronal Structures	O6
Submandibular Gland	H22	Adrenal Gland	A7	Instrument	O7
Oral Cavity	H23	GallBladder	A8		

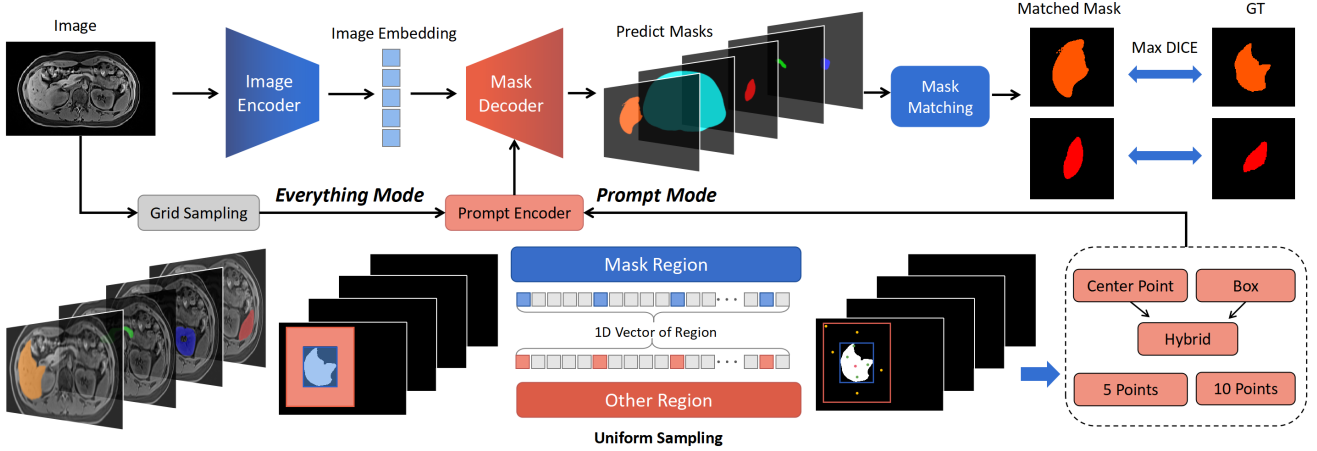


Fig. 5. Testing pipeline of SAM in our study.

Finally, SAM was trained on a massive dataset comprising over one billion masks from 11 million licensed images.

As shown in Fig. 5, SAM mainly contains three components: an image encoder, a prompt encoder, and a mask decoder. The image encoder was, with the backbone of ViT, pre-trained by the masked autoencoder (MAE [83]) technique. It takes one image as input and outputs the image embedding for combinations with subsequent prompt encoding. The prompt encoder consists of dense (masks) and sparse (points, boxes, and text) branches. The dense branch encodes the mask prompts via a convolutional neural network (CNN). For the sparse one, the points and boxes can be represented by positional encoding [84], while the text is embedded by the CLIP [1]. Finally, the mask decoder decodes all the embeddings and predicts the masks.

During testing, SAM supports both automatic *everything* and manual *everything* modes. For the former, the users only have to input an image to SAM, then all the predicted masks will be produced automatically. For the latter, the users should

manually provide some additional hints to SAM, including boxes, points, and texts, to tell SAM more information about the segmented objects. Details of these two modes are presented in the next sub-sections.

In the official GitHub repository⁴, authors provide three types of pre-trained models with different backbone sizes, named *ViT-B*, *ViT-L*, and *ViT-H*. Their model parameters range from small to large. In [4], *ViT-H* shows substantial performance improvements over *ViT-B*; however, the former requires multiplied testing time due to its increased complexity. In our study, we chose *ViT-B* and *ViT-H* as encoders to run the *everything* modes. Besides, for the *prompt* mode, we first explored both *ViT-B* and *ViT-H* using a small amount of our dataset (details refer to IV-C). We found that *ViT-B* achieved similar performance compared with *ViT-H* in this mode. Thus, to shorten the verification time, we only tested the whole dataset under the *prompt* mode using *ViT-B*.

⁴<https://github.com/facebookresearch/segment-anything>

B. Automatic Everything Mode

In the *everything* mode, SAM produces segmentation masks for all the potential *objects* in the whole image without any manual priors. Here, we take the *everything* mode as the first testing strategy, named S_1 . The initial step of the process involves generating a grid of point prompts (*i.e.*, grid sampling) that covers the entire image. Based on the uniformly sampled grid points, the prompt encoder will generate the point embedding and combine it with the image embedding. Then, the mask decoder will take the combination as input and output several potential masks for the whole image. Subsequently, a filtering mechanism is applied to remove duplicate and low-quality masks using the techniques of confidence score, stability evaluation based on threshold jitter, non-maximal suppression (NMS), etc.

C. Manual Prompt Mode

In the *prompt* mode, SAM provides different types of prompts including points, boxes, and texts. The point prompt covers both positive and negative points, which indicate the foreground and background of one object, respectively. The box prompt represents the spatial region of the object that needs to be segmented. Furthermore, the text prompt indicates one sentence (*i.e.*, basic information in terms of position, color, size, etc.) to describe the object. Notably, the text prompt has not been released yet on the official GitHub repository⁴.

As shown in Fig. 5, our prompt mode contains five strategies (S_2 - S_6) including one positive point, five positive points, five positive points with five negative points, one box, and one box with one positive point. We further established a unified rule for point selection to ensure randomness, repeatability, and accuracy. For the positive points selection, a) we first calculated the center of mass of the ground truth (GT) mask (red point in Fig. 5). b) If the center of mass was inside the GT mask, we took the center as the first positive point. c) Then, we directly flattened the GT mask to a one-dimensional vector and obtained the other positive points by adopting the uniform sampling method (green points in Fig. 5). d) If the center of mass was outside the GT mask, all the required positive points would be obtained by performing step c. For the negative points selection, we aimed to avoid selected points that were too distant from the target region. Specifically, we first enlarged the bounding box of the GT by two times. The negative points were generated by even sampling in the non-GT region (yellow points in Fig. 5). Last, for the box selection, we directly adopted the bounding box of the GT mask without any additional operations.

D. Inference Efficiency

In our study, We performed multiple tests (n) on an image using different strategies to obtain a final assessment (see Fig. 5). In SAM’s original code logic and design, the same encoding operation is required on one image n times, which results in poor runtime efficiency in our multi-strategy test scenario. The situation becomes even worse when using high-resolution inputs. Based on this observation, we computed

embedding features of all input images in advance and saved them as intermediate files. Accordingly, the image embeddings could be reused to relieve the computational burden of the inference pipeline. Thereby, the overall efficiency of the SAM testing could be improved by nearly n times. Besides, the more testing strategies of SAM, the more time that could be saved. This can simply be extended to other multi-strategy testing scenarios of SAM.

E. Mask-matching Mechanism for Segmentation Evaluation

SAM generates multiple binary masks for each input image, but not all of them include the corresponding object. Hence, we proposed a mask-matching mechanism to evaluate segmentation performance using SAM in each mode. Specifically, for an object (one of the foregrounds) in a given image, we calculated a set of dice scores $\{\text{DICE}_n\}_{n=1}^N$ between N binary predicted masks $\{\mathbf{P}_n\}_{n=1}^N$ and the GT \mathbf{G} . Then, the one with the highest dice score in the set was selected as the matched predicted mask \mathbf{P} for subsequent segmentation evaluation. This process for obtaining \mathbf{P} can be expressed as follows:

$$\mathbf{P} = \max\{(\mathbf{P}_1 \cdot \mathbf{G}), (\mathbf{P}_2 \cdot \mathbf{G}), \dots, (\mathbf{P}_N \cdot \mathbf{G})\}, \quad (1)$$

where N is the total number of predicted binary masks for an object in one image. The operations (\cdot) and $\max\{\}$ indicate computing a dice score between one predicted mask and the GT, while \max denotes obtaining the predicted mask with the highest dice score.

IV. EXPERIMENTS AND RESULTS

A. Implementation Details

Code implementation and logits. In this study, we implemented the testing pipeline of SAM basically following the official GitHub repository⁴. For our multi-strategy testing scenario, we ran the SAM algorithm n times and extracted image embeddings n times. We observed that the process of image embedding extraction was time-consuming. However, since the same embedding could be reused for different testing strategies, we sought to optimize and accelerate this multi-extraction process. As such, we refactored part of the code. For each test image, we only used the image encoder for feature extraction once and saved the embedded features as an *npz* file. When different testing strategies were applied, only the corresponding *npz* files needed to be loaded, which significantly improved the testing efficiency (approximately $n\times$). Additionally, for the prompt testing, we calculated the required points and boxes once after image embedding and stored them as *npz* files. Thereby, all the prompt testing strategies could directly use the *npz* information without recalculation.

Package versions and features. We used multiple GPUs including NVIDIA GTX 2080Ti with 12GB, NVIDIA GTX 3090 with 24GB and NVIDIA A40 with 48GB for testing. We implemented the SAM with *python* (version 3.8), *PyTorch* (version 2.0.0) and *torchvision* (version 0.15.1). We further adopted: 1) *torch.compile* with the *max-autotune* mode to pack the model; 2) *torch.cuda.amp* to adaptively adjust the types of tensors to Float16 or Float32; 3) *@torch.inference_mode* to replace the common *torch.no_grad*

TABLE III

EXPERIMENTS FOR EVALUATING THE *PROMPT* PERFORMANCE OF ViT-B AND ViT-H ON SIX TASKS. NOTE THAT THE C8 AND A4 SEGMENTATION ARE FROM TASK 6 AND 9 IN [65], RESPECTIVELY.

Metrics	Objects		A1 [30]		A4 [30]		A5 [30]		B3 [71]		B4 [71]		C8 [65]		A4 [65]	
	Model	B	H	B	H	B	H	B	H	B	H	B	H	B	H	
DICE	S_2	78.9 _{20.2}	76.5 _{24.7}	79.5 _{25.1}	79.7 _{26.9}	86.3 _{20.2}	85.7 _{21.8}	92.6 _{11.3}	92.5 _{11.9}	13.7 _{12.8}	11.6 _{12.2}	69.3 _{25.7}	64.8 _{30.4}	78.8 _{25.0}	76.9 _{29.1}	
	S_5	92.2 _{5.04}	92.2 _{5.33}	91.9 _{6.8}	91.6 _{6.7}	92.9 _{8.42}	92.7 _{8.5}	95.1 _{6.2}	94.9 _{6.8}	22.2 _{27.8}	13.7 _{23.8}	84.2 _{11.3}	84.2 _{11.8}	93.5 _{4.5}	93.1 _{5.5}	
HD	S_2	36.1 _{34.4}	41.5 _{41.1}	19.0 _{30.7}	20.7 _{37.4}	8.7 _{18.5}	10.0 _{23.3}	20.0 _{21.4}	18.3 _{18.7}	134.6 _{51.0}	144.0 _{53.0}	34.9 _{52.8}	43.5 _{58.4}	48.6 _{69.6}	56.8 _{87.8}	
	S_5	12.2 _{10.3}	11.8 _{10.2}	3.9 _{3.3}	3.9 _{3.3}	3.4 _{5.6}	3.3 _{5.6}	14.9 _{11.8}	13.9 _{13.3}	45.4 _{25.5}	50.4 _{20.3}	9.3 _{6.2}	9.2 _{6.1}	8.0 _{6.2}	8.1 _{7.3}	

Metrics	Objects		C2 [29]		C3 [29]		C5 [29]		B5 [71]		B6 [71]		O1 [58]		H15 [43]	
	Model	B	H	B	H	B	H	B	H	B	H	B	H	B	H	
DICE	S_2	59.1 _{16.2}	73.2 _{14.9}	34.9 _{10.7}	29.5 _{13.5}	36.8 _{16.9}	46.6 _{24.4}	94.0 _{10.4}	94.0 _{11.5}	21.0 _{19.7}	15.3 _{19.7}	84.2 _{18.2}	86.7 _{17.4}	80.3 _{19.0}	89.5 _{11.8}	
	S_5	88.7 _{3.5}	89.0 _{3.6}	55.2 _{10.7}	47.0 _{13.3}	88.7 _{6.67}	87.8 _{5.1}	96.0 _{5.4}	96.1 _{5.5}	30.3 _{29.1}	21.6 _{27.8}	88.7 _{16.5}	89.9 _{15.7}	90.3 _{5.8}	93.8 _{2.8}	
HD	S_2	54.5 _{21.2}	27.9 _{20.8}	61.3 _{21.3}	64.2 _{23.6}	78.7 _{23.5}	62.7 _{35.3}	14.1 _{25.3}	11.3 _{21.8}	114.8 _{64.3}	142.9 _{71.0}	121.2 _{120.0}	106.5 _{124.5}	96.5 _{83.3}	53.9 _{78.0}	
	S_5	10.4 _{3.6}	9.1 _{4.1}	19.5 _{4.3}	23.6 _{12.0}	6.9 _{3.1}	7.3 _{3.0}	7.7 _{6.4}	6.8 _{5.3}	18.3 _{10.2}	23.6 _{19.1}	72.6 _{91.7}	62.6 _{86.6}	59.5 _{29.3}	31.5 _{18.7}	

to reduce GPU memory occupation and improve inference speed while keeping model calculation precision.

Testing Strategy Design. We design different settings to fully explore the performance of SAM under various testing strategies. We first considered the *everything* mode, which is the key feature of SAM. It can output all the predicted masks for a given image without any manual hints. Then, considering that MIS is a very challenging task, we progressively incorporated various manual prompts to aid in accurate segmentation. The manual prompts included 1) one positive point, 2) five positive points, 3) five positive and five negative points, 4) one box, and 5) one box and one positive point. The manually provided prompts can better guide the SAM to output accurate segmentation results. The above six strategies were represented by the abbreviations S_1 - S_6 .

B. Evaluation Metrics

To fully evaluate SAM’s segmentation performance, we used five common metrics, as shown below:

- 1) **DICE coefficient (DICE, %)** [85]: A similarity measure to evaluate the overlap between the prediction and GT. Ranging from [0, 1], a higher value indicated a better performance of the model.
- 2) **Jaccard similarity coefficient (JAC, %)** [86]: Also known as IOU, is similar to but more demanding than the DICE. It measures the total overlap of ensembles of labels defined on multiple test images and accounts for fractional labels using fuzzy set theory; higher values indicate better performance.
- 3) **Hausdorff Distance (HD, pixel)** [87]: A measure that evaluates the degree of similarity between two sets of points, which can reflect the distance between each point in the prediction to the points in the GT. It is more sensitive to the boundary than DICE.
- 4) **Average Symmetric Surface Distance (ASD, pixel)** [88]: Also referred to as mean surface distance (MSD), is the average surface distance from all points in the prediction to the GT. It measures the surface variation between the segmentation and the GT.
- 5) **Conformity Coefficient (CON)** [89]: It measures the ratio of mis-segmented pixels to correctly segmented pixels using Eq. 2 and has better discrimination in detecting small changes.

$$Con = \begin{cases} 1 - (\theta_{FP} + \theta_{FN})/\theta_{TP} & \text{if } \theta_{TP} > 0 \\ failure & \text{if } \theta_{TP} = 0 \end{cases} \quad (2)$$

where θ_{FP} represents the sum of pixels in the false positive region. θ_{FN} and θ_{TP} indicate the false negatives and true positives, respectively.

C. Model Selection for Different Testing Modes

SAM provides three versions of model with image encoders of different parameter sizes (*ViT-B*, *ViT-L* and *ViT-H*). In this study, we tend to only explore the 1) *ViT-B* with the lowest parameters and the fastest inference speed and 2) *ViT-H* with the highest parameter and the longest inference time, but theoretically optimal performance. Since the *everything* mode is the bright and key function of SAM, we evaluated it using both two models (*everything* with *ViT-B* and *ViT-H*, called S_{1B} and S_{1H}). For the *prompt* mode, we first conducted pre-experiments on part of our whole dataset [29], [30], [43], [58], [65], [71], as shown in Table III. Specifically, we tested two typical strategies (S_2 and S_5) using the DICE and HD metrics. The experiments showed that the two models had no absolute advantage in different datasets or objects. For example, in [29], *ViT-H* outperformed *ViT-B* on the DICE score for C2 (S_2 : 59.1% (B) vs. 73.2% (H)). However, for C8 of [65], *ViT-B* showed better performance than *ViT-H* (S_2 : 69.3% (B) vs. 64.8% (H)). For different structures in the same dataset, e.g., C2, C3, and C4 in [29], there was no winner between *ViT-B* and *ViT-H*. Even for the same structure in different datasets such as the A4 structures in two datasets [30], [65], the performance of these two models remained indistinguishable. Based on the experiments in Table III, our conclusion is that the larger *ViT-H* model does not show a significant advantage over the smaller *ViT-B* model in MIS task under different prompt modes. In other words, we can assume that the two models should achieve similar average results over a large number of medical images. Thus, we chose *ViT-B* as the backbone to test our whole medical dataset to speed up the testing while ensuring that the result reflected SAM’s segmentation ability, which is similar to [16].

D. Model Performance under Different Testing Strategies

In this section, we summarize the results for SAM’s performance under various strategies in terms of the *everything* and

TABLE VI
EXPERIMENTS ON 11 OBJECTS FOR T1-WEIGHTED (BLACK), DIFFUSION-WEIGHTED MRI (RED), AND MULTI-MODAL MRI (BLUE). S: STRATEGIES, AND O: OBJECTS.

Metrics	S/O	H1	H3	H4	H5	H11	H10	A1	A4	A5	H1	H2	P1
DICE ↑	S_{1B}	96.44	41.81	60.32	40.31	69.19	26.70	37.36	39.62	64.62	40.41	28.94	13.07
	S_{1H}	98.77	42.06	60.74	40.78	72.52	35.74	47.73	47.93	73.38	77.68	41.38	33.61
	S_2	96.62	32.96	54.58	39.34	79.80	41.98	81.35	75.57	84.53	84.32	59.25	57.72
	S_3	99.45	44.65	64.84	44.15	85.00	83.18	90.56	88.22	91.32	90.13	80.97	79.71
	S_4	98.73	44.38	64.55	43.72	84.85	83.06	88.97	84.07	88.81	87.36	77.13	72.52
	S_5	99.65	44.73	64.93	45.38	89.69	90.93	92.02	90.35	91.95	91.62	82.80	81.16
	S_6	99.49	43.63	64.07	44.08	88.03	90.48	91.68	90.02	92.00	90.97	82.50	80.07
JAC ↑	S_{1B}	94.65	28.95	43.89	26.42	62.28	21.61	27.78	34.33	58.98	34.44	18.70	9.91
	S_{1H}	97.77	29.15	44.19	26.73	65.23	29.05	38.09	42.49	67.39	69.41	30.78	26.22
	S_2	95.16	22.45	40.03	25.97	70.71	31.68	71.65	66.54	77.27	75.40	46.32	45.74
	S_3	98.94	31.91	48.30	29.13	76.29	71.85	83.22	80.04	85.18	82.93	69.93	69.59
	S_4	97.57	31.59	48.01	28.84	75.52	71.76	80.74	74.22	81.14	78.71	64.91	59.99
	S_5	99.31	32.03	48.47	30.22	82.22	83.65	85.56	82.93	85.89	85.17	72.44	71.42
	S_6	99.04	30.91	47.62	29.17	79.95	82.96	85.01	82.43	86.00	84.21	72.00	70.33
HD ↓	S_{1B}	7.16	43.04	43.06	44.15	47.33	71.50	97.50	86.13	39.29	49.27	74.86	113.25
	S_{1H}	4.90	46.55	44.86	46.49	39.20	85.41	80.68	71.65	26.87	28.20	61.29	70.85
	S_2	7.26	47.50	45.91	44.56	10.76	49.96	31.25	22.64	9.31	26.48	45.08	35.40
	S_3	3.95	34.98	31.43	32.02	4.50	11.72	13.95	6.69	3.59	17.22	17.76	12.22
	S_4	8.37	30.88	27.52	28.37	6.95	19.91	17.74	15.52	7.73	22.94	24.76	23.99
	S_5	2.80	35.98	29.64	25.49	3.48	9.10	11.27	4.48	3.37	13.88	13.97	11.03
	S_6	3.13	36.83	33.68	31.64	3.69	9.72	11.79	5.08	3.19	15.81	14.39	11.70
ASD ↓	S_{1B}	1.61	9.74	14.40	17.45	39.96	40.14	26.30	19.67	13.75	26.58	19.73	88.64
	S_{1H}	0.76	10.50	14.71	18.15	21.48	36.58	20.48	14.79	8.36	9.78	15.77	39.68
	S_2	0.99	8.48	12.67	15.13	1.80	7.07	3.56	2.51	1.73	5.05	7.07	6.70
	S_3	0.21	6.58	9.86	11.58	1.39	1.16	1.81	1.32	1.09	2.56	3.22	2.38
	S_4	0.46	5.02	8.00	9.09	1.37	0.92	1.88	1.34	1.20	2.89	2.84	2.62
	S_5	0.17	6.87	9.67	9.21	1.08	0.66	1.72	1.12	1.07	2.42	3.00	2.23
	S_6	0.19	7.04	10.59	11.32	1.19	0.67	1.82	1.16	1.07	2.48	3.06	2.32
CON ↑	S_{1B}	56.54	-297.59	-326.93	-515.28	-994.02	-8905.55	-1257.45	-3065.01	-2968.52	-4656.07	-694.63	-6675.02
	S_{1H}	95.34	-278.61	-42.81	-364.54	-5389.26	-4043.19	-889.61	-2524.15	-2227.53	-343.54	-484.72	-4233.95
	S_2	-1570.78	-94709.54	-13411.04	-948.31	-524.17	-697.63	-17.81	-163.25	-492.69	45.40	-150.42	-822.79
	S_3	98.87	-255.54	-12.79	-210.14	51.01	57.63	78.17	69.19	80.03	75.24	41.70	-56.14
	S_4	97.35	-262.21	-14.91	-223.95	56.04	56.82	73.70	54.13	73.52	66.06	25.30	-114.18
	S_5	99.30	-255.94	-12.23	-191.14	71.66	79.46	82.01	76.00	83.04	80.15	47.05	-26.63
	S_6	98.88	-263.48	-17.64	-211.22	65.64	78.27	81.16	76.10	83.14	78.30	39.10	-81.05

TABLE VII
EXPERIMENTS ON T2-WEIGHTED MRI. S: STRATEGIES, AND O: OBJECTS.

Metrics	S/O	H3	H4	H5	H6	H7	H8	H9	A1	A4	A5	P1
DICE ↑	S_{1B}	35.79	24.85	38.06	35.03	19.47	14.38	25.45	30.31	72.97	81.18	12.90
	S_{1H}	43.63	28.72	45.34	42.30	33.82	16.81	33.11	37.40	79.73	85.30	33.37
	S_2	43.40	28.80	47.78	33.20	50.27	19.95	48.64	73.69	87.22	89.99	63.73
	S_3	50.11	36.78	63.36	61.99	72.33	61.90	78.55	90.44	93.70	94.14	85.58
	S_4	49.78	35.30	62.22	62.00	68.58	50.24	74.92	87.39	91.83	92.96	77.78
	S_5	51.85	38.37	67.28	67.29	80.23	60.61	87.52	92.63	94.98	94.76	86.61
	S_6	50.63	37.42	64.47	62.68	78.14	57.12	85.77	92.05	94.75	94.76	86.05
JAC ↑	S_{1B}	24.53	15.50	25.22	24.86	13.38	8.03	20.53	21.46	68.68	76.45	9.52
	S_{1H}	30.69	17.93	30.82	31.29	24.18	9.46	26.58	28.15	75.11	80.24	24.89
	S_2	30.49	17.97	33.11	23.70	37.39	11.52	39.55	62.89	81.21	84.53	50.64
	S_3	36.73	23.98	48.44	49.37	59.10	47.81	67.42	83.23	88.75	89.62	76.98
	S_4	36.26	22.81	47.33	49.34	54.03	35.13	62.20	78.53	85.87	87.67	65.85
	S_5	38.37	25.25	53.04	55.31	68.46	48.80	78.94	86.72	90.90	90.53	78.32
	S_6	37.19	24.49	49.74	50.28	65.74	44.87	76.57	85.77	90.33	90.54	77.67
HD ↓	S_{1B}	58.19	60.67	60.70	57.20	62.58	71.85	43.76	107.28	37.50	21.54	146.27
	S_{1H}	48.45	53.01	54.07	50.74	49.17	71.26	35.64	106.70	26.02	15.45	100.80
	S_2	44.47	46.22	46.92	41.15	28.89	67.91	23.77	46.30	11.90	7.40	45.58
	S_3	35.45	33.30	30.15	18.84	12.84	31.71	8.98	18.19	4.14	3.35	15.21
	S_4	32.93	31.53	28.02	24.66	15.17	40.20	9.93	23.43	9.71	6.83	32.28
	S_5	36.02	32.43	25.49	15.92	8.46	17.11	3.52	14.06	2.86	3.38	12.84
	S_6	36.79	34.43	29.62	18.25	10.17	19.94	4.73	14.88	3.12	3.11	13.39
ASD ↓	S_{1B}	20.48	25.93	29.00	29.54	30.00	40.21	25.47	32.53	8.09	6.98	110.85
	S_{1H}	14.23	19.75	23.72	23.60	20.44	39.19	18.37	30.29	5.06	4.18	48.82
	S_2	11.35	14.15	17.82	13.88	7.21	26.25	7.07	5.33	1.28	1.08	7.65
	S_3	6.60	7.50	8.42	2.61	2.64	4.44	1.40	1.70	0.70	0.96	2.60
	S_4	5.55	6.45	6.54	2.22	2.47	4.09	1.53	1.82	0.73	1.00	3.09
	S_5	6.97	7.33	6.77	2.58	1.98	4.11	0.90	1.53	0.59	0.92	2.48
	S_6	7.14	7.95	8.31	3.02	2.20	4.34	1.00	1.57	0.62	0.93	2.55
CON ↑	S_{1B}	-10941.63	-1598.77	-1891.75	-4144.88	-5129.81	-5355.79	-3547.06	-2277.28	-1555.34	-1794.48	-8315.50
	S_{1H}	-1541.34	-845.51	-477.59	-3663.48	-3715.22	-2787.29	-2873.74	-1629.80	-1735.66	-1812.19	-7450.82
	S_2	-7976.26	-2769.52	-795.83	-2028.98	-1018.82	-2038.65	-1088.06	-55.92	-63.50	-396.92	-111.44
	S_3	-559.72	-388.24	-60.61	-228.14	-47.20	-133.13	-5.71	77.19	85.05	87.18	55.34
	S_4	-544.99	-420.61	-69.27	-237.34	-33.87	-205.77	4.06	68.46	79.63	84.22	26.43
	S_5	-522.65	-338.17	-53.42	-399.86	38.51	-835.16	59.41	83.15	81.62	89.13	58.66
	S_6	-590.91	-359.25	-54.60	-372.93	28.55	-869.48	49.71	81.67	88.36	89.11	55.07

- *Prompt* modes: Experimental results reported in Table IV-IX show that performances under five different prompts (S_2 - S_6) are better than that of the best *everything* mode (i.e., S_{1H}). This indicates that the manual hints can refine SAM's ability to recognize objects in medical images. Further more, different

prompts have different effects on segmentation results. The experiments under S_2 showed the worst performance, likely due to the limited information provided by only one positive point. However, when four additional positive points were added to S_3 , we observed a significant improvement in the

TABLE VIII
EXPERIMENTS OF 11 OBJECTS ON US (C2-C5, BLACK), X-RAY (C1-C7, RED), COLONOSCOPY (P2-O7, BLUE) AND FUNDUS (H12-H16). S: STRATEGIES, AND ST: OBJECTS.

Metrics	S/St	H28	C2	C3	C5	C1	C7	P2	O1	O7	H12	H15	H16
DICE ↑	S_{1B}	31.52	19.71	20.34	13.35	18.02	9.56	47.14	49.49	45.59	65.14	35.84	14.60
	S_{1H}	48.56	30.16	28.37	17.95	30.64	64.42	74.33	71.29	75.55	99.22	72.84	20.10
	S_2	66.57	59.07	34.88	36.79	50.07	93.25	82.69	81.63	80.93	99.30	77.05	21.70
	S_3	90.70	87.78	56.18	81.67	90.89	95.13	92.61	90.64	91.41	99.27	92.38	20.55
	S_4	85.73	79.73	53.95	75.76	80.25	94.36	90.54	89.08	88.76	99.09	89.65	21.04
	S_5	90.12	88.70	55.17	88.68	84.68	95.32	92.10	89.94	90.89	99.15	89.88	20.55
	S_6	90.30	88.92	55.10	89.36	89.11	95.11	92.22	90.68	90.89	99.22	90.15	21.02
JAC ↑	S_{1B}	24.21	11.58	11.75	7.37	12.00	7.36	41.19	41.53	39.38	64.22	30.88	8.14
	S_{1H}	39.59	18.62	16.81	10.35	20.47	57.85	65.46	63.94	67.36	98.46	67.44	11.23
	S_2	54.58	43.76	21.65	24.08	34.49	87.80	73.81	73.13	71.58	98.62	67.16	12.22
	S_3	83.22	78.41	39.53	70.37	83.66	90.97	86.69	84.46	84.92	98.55	86.15	11.49
	S_4	75.63	66.74	37.37	61.92	67.47	89.58	83.33	81.66	80.87	98.20	82.07	11.80
	S_5	82.46	79.87	38.83	80.19	74.59	91.31	86.16	83.95	84.26	98.32	82.32	11.49
	S_6	82.70	80.20	38.64	81.02	81.03	90.94	86.39	84.67	84.27	98.45	82.78	11.80
HD ↓	S_{1B}	163.70	87.77	77.81	90.38	543.53	1977.68	475.73	214.44	326.06	147.05	940.49	344.80
	S_{1H}	127.29	83.21	71.32	98.25	424.09	829.27	323.69	145.66	189.25	4.28	315.64	320.42
	S_2	77.62	54.49	61.27	78.65	355.66	257.39	277.91	111.48	150.49	84.68	149.21	262.85
	S_3	24.62	12.85	25.12	26.00	127.21	180.92	120.61	65.39	58.05	35.73	62.10	234.64
	S_4	44.23	26.88	26.13	23.14	224.96	355.63	188.60	93.96	136.86	112.20	111.80	243.34
	S_5	20.86	10.44	19.52	6.91	90.10	159.31	99.36	59.50	49.88	4.56	67.78	299.22
	S_6	21.61	10.21	20.67	7.00	89.80	175.42	103.72	60.51	52.50	37.85	64.53	253.24
ASD ↓	S_{1B}	63.66	33.22	23.34	28.88	358.81	1159.43	221.00	67.72	128.72	84.54	221.48	143.62
	S_{1H}	44.62	26.72	18.94	24.90	195.39	205.38	58.68	36.67	33.48	2.01	83.27	124.88
	S_2	12.49	7.04	13.08	9.20	46.15	26.90	22.94	11.39	17.54	1.68	26.36	91.72
	S_3	3.35	2.30	6.28	2.33	9.08	21.39	9.62	4.86	7.18	1.87	9.51	83.08
	S_4	4.02	2.90	6.27	2.72	13.48	22.74	9.91	4.97	7.34	2.23	9.73	84.11
	S_5	3.73	2.27	5.78	1.76	15.09	21.45	11.07	5.77	7.93	2.18	12.53	114.20
	S_6	3.65	2.21	6.26	1.66	12.03	21.92	10.70	5.31	7.90	1.96	12.07	93.73
CON ↑	S_{1B}	-3666.90	-2878.56	-6531.41	-4343.93	-1587.34	-147281.30	-93303.97	-3990.21	-22897.60	-5627.67	-2508.67	-169159.66
	S_{1H}	-993.91	-520.69	-610.74	-1100.08	-6036.32	-56044.96	-65608.28	-523.19	-5335.91	-98.43	-787.11	-754.04
	S_2	-129.27	-77.03	-339.37	-380.69	-129.19	84.18	-370.09	-23.68	-127.29	98.60	-7.92	-650.83
	S_3	79.01	71.73	-64.44	49.15	79.16	89.91	83.16	71.39	78.59	98.53	82.85	-700.95
	S_4	65.02	47.39	-79.82	31.15	49.01	88.19	77.75	68.87	70.74	98.16	74.62	-679.21
	S_5	76.51	74.13	-79.85	72.03	60.01	90.33	79.29	-862.40	-412.32	98.28	75.72	-700.65
	S_6	77.42	74.74	-76.76	75.61	73.86	89.83	62.41	68.89	30.46	98.42	76.30	-685.97

TABLE IX
EXPERIMENTS ON DERMOSCOPY (O2, BLACK), MICROSCOPY (O3, RED), HISTOPATHOLOGY (O4, BLUE) AND ELECTRON MICROSCOPY (O5-O6, GREEN). S: STRATEGIES, AND O: OBJECTS.

Metrics	S/O	O2	O3	O4	O5	O6
DICE ↑	S_{1B}	47.43	55.94	41.41	64.61	54.63
	S_{1H}	61.26	75.45	75.26	81.05	61.54
	S_2	76.06	84.34	74.31	79.78	78.57
	S_3	88.29	91.31	91.63	86.81	84.37
	S_4	84.57	89.35	87.51	85.24	81.44
	S_5	87.47	91.76	91.40	89.68	86.99
	S_6	87.56	91.60	90.73	88.51	86.20
JAC ↑	S_{1B}	37.96	49.72	35.02	56.20	48.21
	S_{1H}	50.93	67.24	68.69	71.55	55.26
	S_2	64.40	75.38	63.04	68.54	68.58
	S_3	79.49	84.67	85.15	77.56	74.76
	S_4	74.12	81.59	78.83	75.01	70.71
	S_5	78.52	85.26	84.82	81.59	78.18
	S_6	78.57	85.02	83.77	79.88	77.11
HD ↓	S_{1B}	947.16	82.76	299.05	172.33	126.14
	S_{1H}	697.27	33.55	126.99	27.52	95.13
	S_2	444.84	17.00	89.15	15.32	20.55
	S_3	307.99	13.30	50.98	7.26	14.71
	S_4	465.14	17.11	84.32	12.02	26.25
	S_5	274.31	6.93	30.33	6.00	7.52
	S_6	283.00	7.67	32.58	6.43	8.40
ASD ↓	S_{1B}	294.80	51.83	129.00	65.56	72.31
	S_{1H}	208.92	11.19	33.00	13.84	55.60
	S_2	90.01	2.71	13.44	4.28	3.28
	S_3	37.66	1.52	4.50	2.85	1.73
	S_4	41.83	1.71	5.06	3.17	1.78
	S_5	44.86	1.56	4.91	2.34	1.50
	S_6	42.54	1.58	5.33	2.55	1.63
CON ↑	S_{1B}	-5446.16	-11914.26	-2670.21	-8245.21	-7486.62
	S_{1H}	-518.08	-2357.35	-1351.79	-630.93	-6655.50
	S_2	-0.67	-16.55	-42.11	-0.14	-159.28
	S_3	72.40	78.07	79.76	65.52	54.34
	S_4	60.83	72.35	67.53	62.00	42.09
	S_5	68.04	80.91	79.65	76.29	64.24
	S_6	69.19	80.38	77.75	72.58	61.12

segmentation performance, *e.g.*, the brain tumor in (r_3, S_2) to (r_3, S_3) of Fig. 7. Based on these five positive points, we also attempted to add five negative points to provide SAM with some background information (S_4). While this approach could theoretically improve the performance, we observed that the addition of negative points slightly decreased the segmentation

performance in some cases, *e.g.*, the heart in (r_7, S_3) to (r_7, S_4) of Fig. 7. This is due to the complexity of medical images, in which the foreground and background are easily confused. If some background points similar to the foreground ones are selected, it will generate incorrect guidance for SAM. This suggests that for medical images, we have to rely on professional knowledge to carefully (rather than randomly) select point prompts, especially background points, in order to better achieve stable performance improvement. In addition to the point prompts, we also evaluated the performance prompted by objects' bounding boxes (S_5). It can be shown that S_5 achieved better results than S_2 - S_4 in most cases. This phenomenon indicates that the information contained in the box prompts may be richer than that contained in the point prompts. Specifically, different from the point prompts that provide only pixel-level information, box prompts provide vital region-level position information about the object. Such position and region hints can better drive the SAM to segment the objects in medical images, *e.g.*, the left ventricle in S_2 to S_5 of Fig. 7 (r_5). We then added one positive point to the box (S_6) and expected the introduction of this point to further improve the performance of S_5 . However, we notice that after adding one point prompt to the box prompt, the performance instead has no significant changes. As shown in Table X, compared with S_5 , averaged DICE drop on 9 modalities and improve on 7 modalities under S_6 . This is likely related to SAM's ability to support hybrid prompts. This limitation could be attributed to the prompt encoder used by SAM. To improve the segmentation performance of hybrid prompts, it may be necessary to enhance the prompt encoder's ability to more efficiently promote the interaction of different prompt information during both training and testing.

TABLE X

RESULTS OF DIFFERENT MODALITY DATA UNDER DIFFERENT TESTING STRATEGIES. M1: CT, M2: MRI, M3: MULTI-MODAL MRI, M4: CINE-MRI, M5: CMR, M6: T1-WEIGHTED MRI, M7: T2-WEIGHTED MRI, M8: DIFFUSION-WEIGHTED MRI, M9: US, M10: X-RAY, M11: COLONOSCOPY, M12: FUNDUS, M13: HISTOPATHOLOGY, M14: DERMOSCOPY, M15: MICROSCOPY, M16: ELECTRON MICROSCOPY. S: STRATEGIES, AND O: OBJECTS.

Metrics	S/O	M1	M2	M3	M4	M5	M6	M7	M8	M9	M10	M11	M12	M13	M14	M15	M16
DICE \uparrow	S_{1B}	60.640.7	38.641.0	28.718.8	37.637.1	30.636.0	76.132.1	30.525.4	40.439.1	26.627.3	11.022.6	47.038.7	41.438.5	35.038.9	55.941.0	62.237.3	47.433.4
	S_{1H}	68.037.1	44.140.7	41.227.7	52.533.1	46.433.3	79.330.1	38.125.3	77.726.0	40.330.5	58.537.0	74.129.4	75.331.9	68.737.4	75.528.8	76.327.8	61.330.8
	S_2	72.133.7	63.732.6	59.224.2	66.726.3	65.525.5	81.427.7	42.125.4	84.315.4	58.335.1	85.718.1	81.319.7	74.320.9	72.426.9	84.315.6	79.516.9	76.118.2
	S_3	85.420.4	79.421.1	80.913.6	79.918.3	77.419.0	87.021.0	59.024.5	90.118.4	85.112.6	94.45.1	91.38.9	91.66.7	85.422.4	91.37.1	86.29.9	88.35.8
	S_4	83.321.1	76.222.4	77.114.9	75.919.3	72.820.2	86.120.9	56.723.6	87.410.0	80.012.6	91.97.5	89.19.5	87.59.2	83.122.3	89.48.2	84.39.9	84.08.4
	S_5	88.418.1	78.825.3	82.513.2	80.918.3	77.920.0	87.820.6	62.225.4	91.67.7	93.51.0	93.57.3	90.710.8	91.4.9	83.222.3	91.8.8	89.0.6	87.58.0
JAC \uparrow	S_{1B}	55.311.1	33.537.9	18.516.9	30.834.2	24.924.4	70.435.4	21.121.5	34.437.6	19.231.8	8.219.8	40.338.1	35.037.0	30.138.0	49.738.5	54.234.0	38.031.8
	S_{1H}	62.138.1	38.137.8	30.727.4	42.732.3	36.830.9	74.033.8	27.022.6	69.428.2	30.829.8	51.338.4	66.131.4	68.733.0	63.138.3	67.229.2	67.229.2	50.930.9
	S_2	65.535.1	54.332.1	46.324.9	55.628.7	53.927.7	75.831.2	30.423.5	75.419.2	45.725.8	78.522.2	72.323.0	63.023.9	63.029.9	75.418.5	68.518.8	64.429.0
	S_3	78.824.1	69.722.9	69.917.1	70.023.0	66.823.7	81.826.3	46.224.3	82.911.9	75.91.1	89.76.6	85.012.1	85.29.9	79.124.0	84.710.2	76.912.9	79.59.0
	S_4	75.724.9	65.823.8	64.818.0	64.723.2	61.023.9	80.326.0	43.423.7	78.713.2	68.315.9	85.710.5	81.413.2	78.812.8	75.624.3	81.611.5	74.012.8	74.112.0
	S_5	82.721.2	70.325.7	72.416.5	71.422.7	67.824.1	82.925.7	50.026.6	85.210.3	76.616.3	88.49.9	84.413.8	84.810.4	75.824.1	85.39.0	80.89.3	78.511.3
HD \downarrow	S_{1B}	89.5104.6	108.098.6	75.526.8	45.551.2	73.274.9	28.645.5	63.447.9	49.331.2	135.595.4	1727.51426.4	307.6305.3	299.0412.0	842.6800.5	82.8119.8	161.0303.3	947.2922.4
	S_{1H}	75.064.8	98.989.7	61.533.2	35.049.8	56.576.6	24.941.4	53.739.2	28.223.6	111.892.2	758.6899.4	190.4250.8	127.0605.7	301.7540.9	33.559.8	44.1124.8	697.3888.4
	S_2	54.575.8	45.883.5	44.928.6	16.417.0	21.930.5	17.823.9	43.028.2	26.515.0	73.061.9	274.6278.2	152.3190.3	89.2154.6	157.8185.6	17.031.3	16.628.1	444.8573.2
	S_3	21.220.1	16.529.1	17.713.6	6.45.3	8.17.4	10.614.6	26.524.9	17.29.8	23.421.5	171.5161.6	67.276.8	51.0122.4	78.578.6	13.366.4	9.123.7	308.0400.9
	S_4	35.943.9	23.934.9	24.814.8	11.94.5	16.014.7	13.314.0	27.624.5	22.910.9	37.530.1	332.8264.7	129.118.2	84.3128.5	125.380.4	17.134.8	15.531.9	465.1496.0
	S_5	14.921.4	13.721.0	13.98.1	5.44.1	7.26.0	9.113.8	23.621.8	13.98.8	17.816.5	147.2159.0	58.370.4	30.358.8	88.588.2	6.911.8	6.45.6	274.3369.7
ASD \downarrow	S_{1B}	17.825.4	13.821.0	14.38.9	5.84.5	7.46.4	10.115.0	25.523.9	15.810.1	18.417.2	160.4167.9	60.670.4	32.667.9	82.672.2	7.716.9	6.99.4	283.0375.9
	S_{1H}	30.344.8	33.940.4	20.915.3	24.833.9	42.049.3	10.328.0	30.933.4	26.620.2	51.043.1	1019.8996.3	119.8187.2	129.0271.7	207.1202.5	51.8100.2	67.2159.1	294.8356.8
	S_2	21.336.3	25.731.1	16.212.3	13.023.3	21.032.4	7.620.0	22.121.5	9.812.2	37.034.9	203.6291.6	37.272.6	33.097.3	83.7147.7	11.244.2	24.186.4	208.9303.3
	S_3	7.315.2	6.010.1	7.15.3	3.15.0	4.48.0	3.65.5	13.210.3	5.01.9	11.512.4	30.328.1	16.224.4	13.416.7	31.934.0	2.74.3	4.09.9	90.0110.6
	S_4	2.34.3	4.115.5	3.22.1	1.51.1	2.11.6	2.34.2	5.54.7	2.61.7	3.52.2	19.255.4	6.76.4	4.52.2	16.725.1	1.51.6	2.61.3	37.735.6
	S_5	2.24.1	4.115.5	2.81.8	1.51.0	2.11.5	2.13.4	4.74.1	2.93.3	4.02.7	21.154.4	6.95.9	5.15.9	17.027.3	1.71.9	2.81.4	41.899.3
	S_6	2.14.6	4.415.8	3.01.9	1.41.0	1.91.6	2.13.9	5.14.5	2.41.4	3.64.4	20.354.4	7.68.1	4.92.1	22.455.6	1.61.6	2.11.0	44.945.6
	S_6	2.34.5	4.215.6	3.11.9	1.51.1	2.01.7	2.44.3	5.64.8	2.51.5	3.62.5	20.254.5	7.48.2	5.37.0	20.028.6	1.61.8	2.31.2	42.539.7

TABLE XI

ABLATION STUDY ON THE NUMBER OF POINTS IN EVERYTHING MODE.

	8^2	16^2	32^2	64^2	128^2	256^2
O4 [79]	42.344.1	70.437.4	76.332.5	77.831.1	78.730.4	79.130.2
O4 [33]	55.642.4	70.934.7	74.231.5	76.330.0	77.129.1	77.628.6
O5 [38]	31.839.3	71.131.4	81.120.1	81.519.1	81.718.6	81.718.3
O6 [73]	21.338.0	45.744.1	61.540.1	64.438.4	65.437.8	65.837.5

The DICE boxplot in Fig. 6 supports the above conclusion more intuitively. For example, after adding more positive points, the segmentation performance will be improved and the standard deviations will go down (row 2 vs. row 3). Box prompt shows better performance that the points prompts (row 5 vs. rows 2-4). The hybrid prompt has a slight decline compared with the box prompt in the DICE average value, but for some objects, it can reduce the standard deviation and improve the stability (e.g., H18 and H21, row 5 vs. row 6). It can also be observed from Fig. 6 that less than 20 medical objects are perfectly supported by SAM (e.g., H1, H12, C2, etc. with large mean ($> 90\%$) and low standard deviations ($< 10\%$) in DICE).

E. Performance of Medical Images with Different Modalities

In Table X, we summarized SAM’s performance for data with different modalities. In the *everything* mode (S_{1H}), the T1-weighted MRI, diffusion-weighted MRI, colonoscopy, fundus, dermoscopy, and microscopy modalities achieved a DICE score of over 70% but with large standard deviations. This can prove the instability of the *everything* mode. For the *prompt* mode, X-ray achieved the best performance among all the modalities. In general, based on criterion of high mean ($> 85\%$) and low standard deviation ($< 10\%$) in DICE, SAM can only fit 6 modalities (M8, M10, M12, M14, M15, M16). However, as different modalities contain different types of objects, it may be unfair to compare the performance of different modalities directly.

For a pair comparison, we turn to evaluate the SAM’s performance of the same object with different modalities, which

could directly reflect the difference in SAM’s segmentation ability for different modalities. We conducted five groups of comparisons to analyze this issue, taking experiments with box prompts S_5 for comparison. **1) H1 in T1-weighted and Diffusion-weighted MRI (Table VI).** On T1-weighted MRI, SAM perfectly segmented the H1 (brain) with a DICE score of 99.65%. However, for diffusion-weighted MRI, the DICE score was only 91.62%, with a large gap of 8.03%. **2) C1 in CT (Table IV) and X-ray (Table VIII).** For these two modalities, the segmentation performance of C1 exhibited significant differences. Specifically, for CT, C1 achieved a DICE score of 90.15%. However, the DICE score of X-rays dropped by 5.47%. **3) C2 and C3 in Cine-MRI (Table V), CMR (Table V) and US (Table VIII).** The experiments showed that for C2, the average DICE score of Cine-MRI and CMR were similar (92.45% vs. 91.92%). However, its performance in the US was obviously poorer (88.70%). For C3, the segmentation performance varied among the three modalities (62.62%, 56.78% vs. 55.17%, respectively). Overall, cine-MRI achieved better performance in both structures of the heart than the other two modalities, whereas US was the worst performer. **4) A1, A4, A5 in CT (Table IV), MRI (Table V), T1-(Table VI) and T2-weighted MRI (Table VII).** SAM’s performance was satisfactory in segmenting the three structures in these modalities. All the DICE scores (12 groups, 3 structures \times 4 modalities) were over 90%. Besides, the performance of the three structures did not vary greatly in CT and the three MRI modalities. **5) A7-A12 in CT (Table IV) and MRI (Table V).** As shown in these tables, the DICE scores of the six structures in the two modalities were a) 74.16%, 87.72%, 84.46%, 84.98%, 91.92%, 89.73% and b) 69.55%, 87.97%, 81.12%, 82.62%, 90.86%, 87.44%, respectively. Clearly, SAM performed better on CT than on MRI for these six structures. In general, SAM can perform well on the CT and MRI in most cases. However, SAM’s performance is easily affected by many factors, for example, in diffusion-weighted MRI, the DICE of the same object type drops significantly. Besides, for the US dataset, the performance of SAM is poor due to the low image quality.

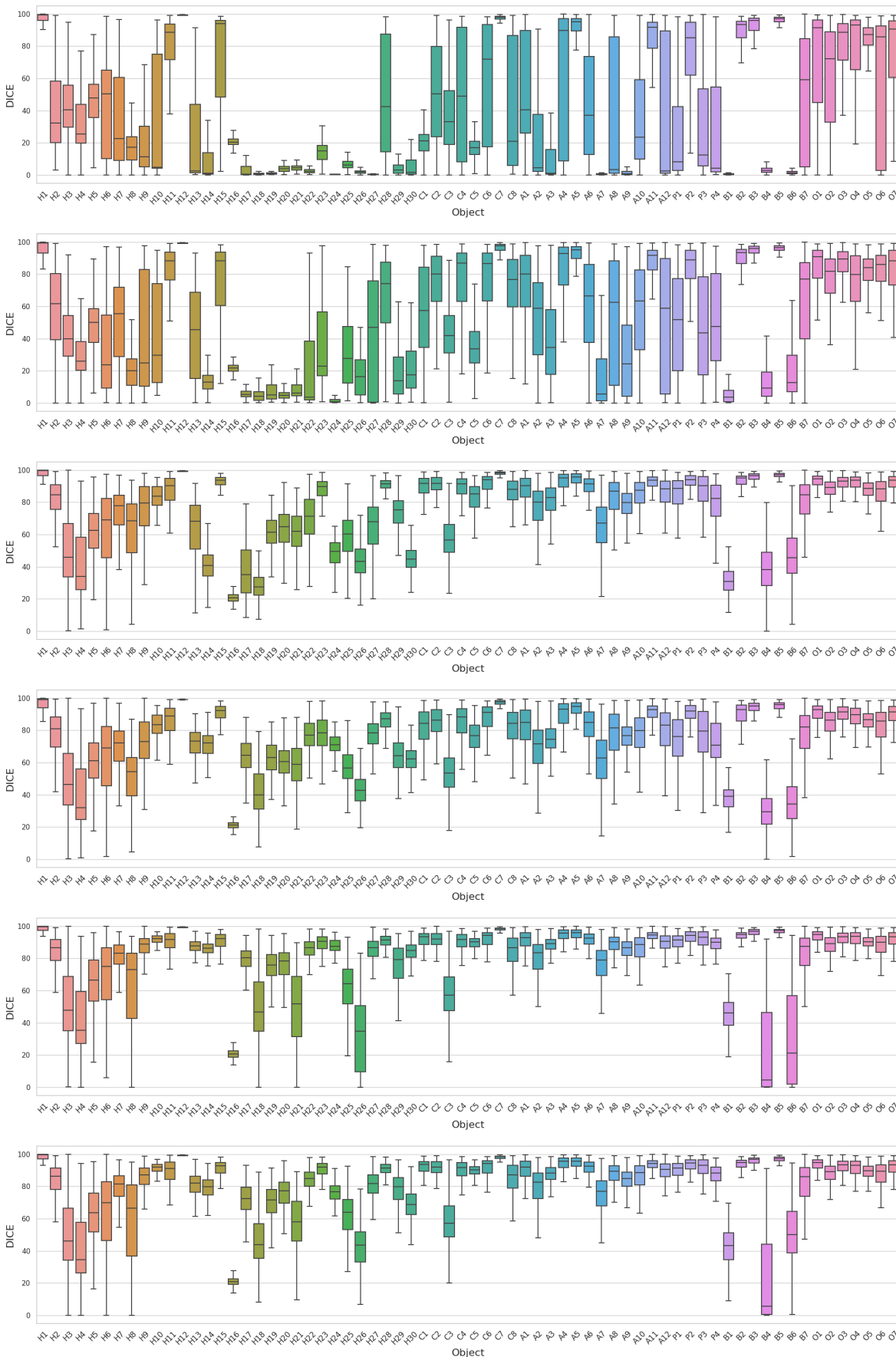


Fig. 6. DICE boxplot of different testing strategies. From top to bottom: S_{1H} , S_2 , S_3 , S_4 , S_5 and S_6

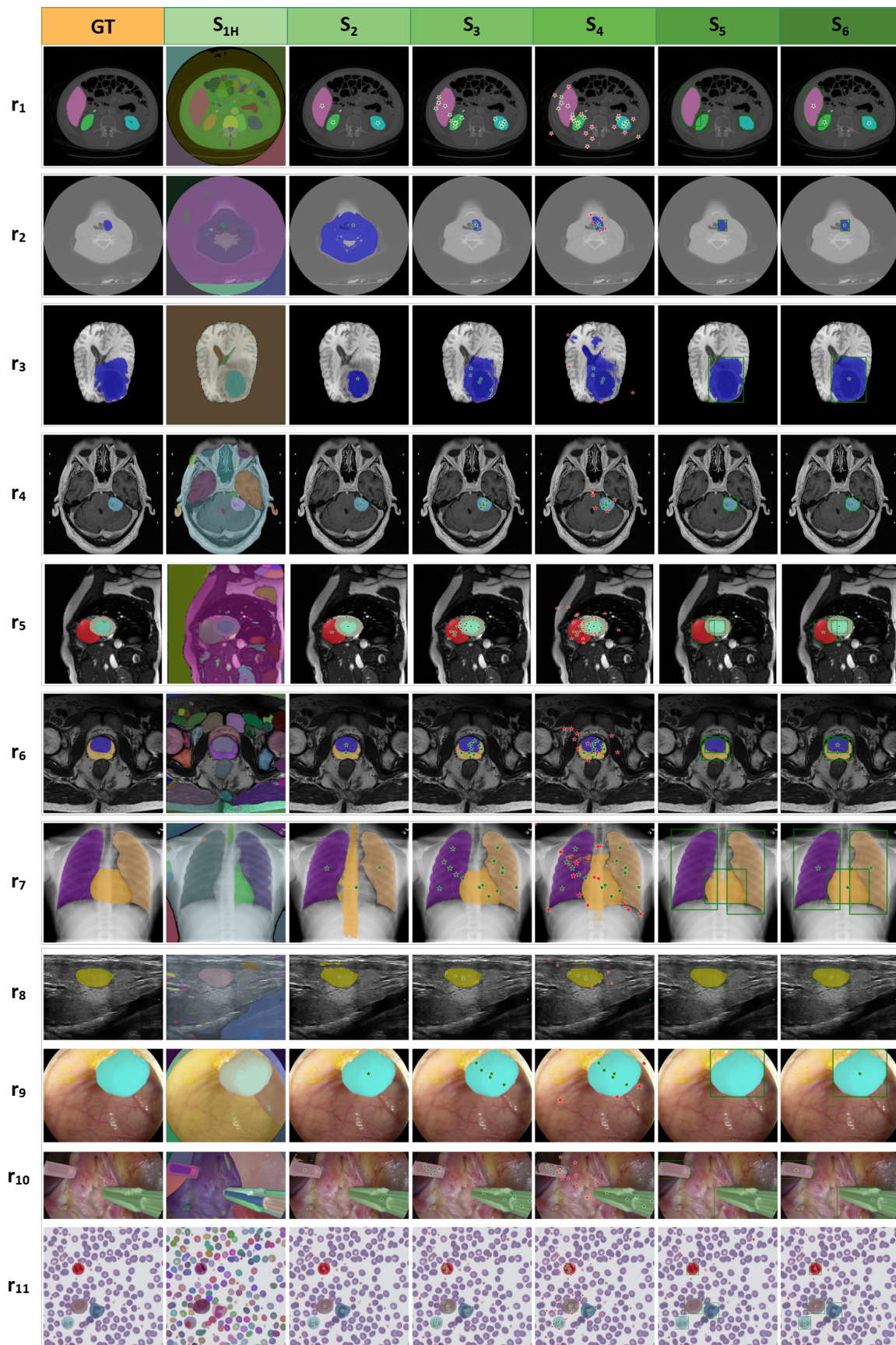


Fig. 7. Typical good cases of SAM (r : row). r_1, r_2 : CT, r_3 : Multi-modal MRI, r_4 : T1-weighted MRI, r_5 : Cine MRI, r_6 : T2-weighted MRI, r_7 : X-ray, r_8 : US, r_9, r_{10} : Colonoscopy, r_{11} : Microscopy. Green and red stars represent positive and negative point prompts, respectively. Green box indicates box prompt.

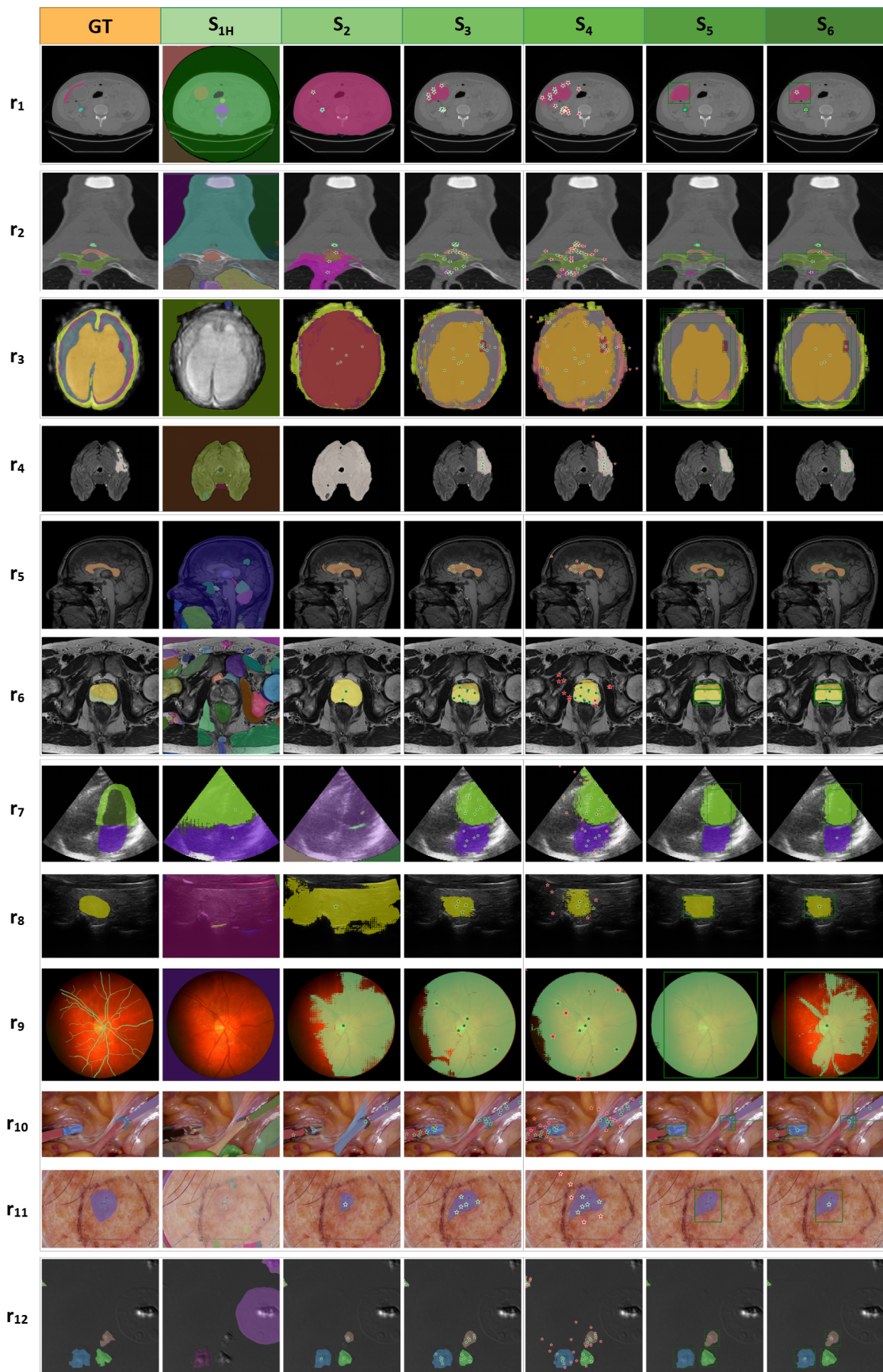


Fig. 8. Typical bad cases of SAM (r : row). r_1, r_2 : CT, r_3, r_6 : T2-weighted MRI, r_4 : Multi-modal MRI, r_5 : T1-weighted MRI, r_7, r_8 : US, r_9 : Fundus, r_{10}, r_{11} : Colonoscopy, r_{12} : Microscopy. Green and red stars represent positive and negative point prompts, respectively. Green box indicates box prompt.

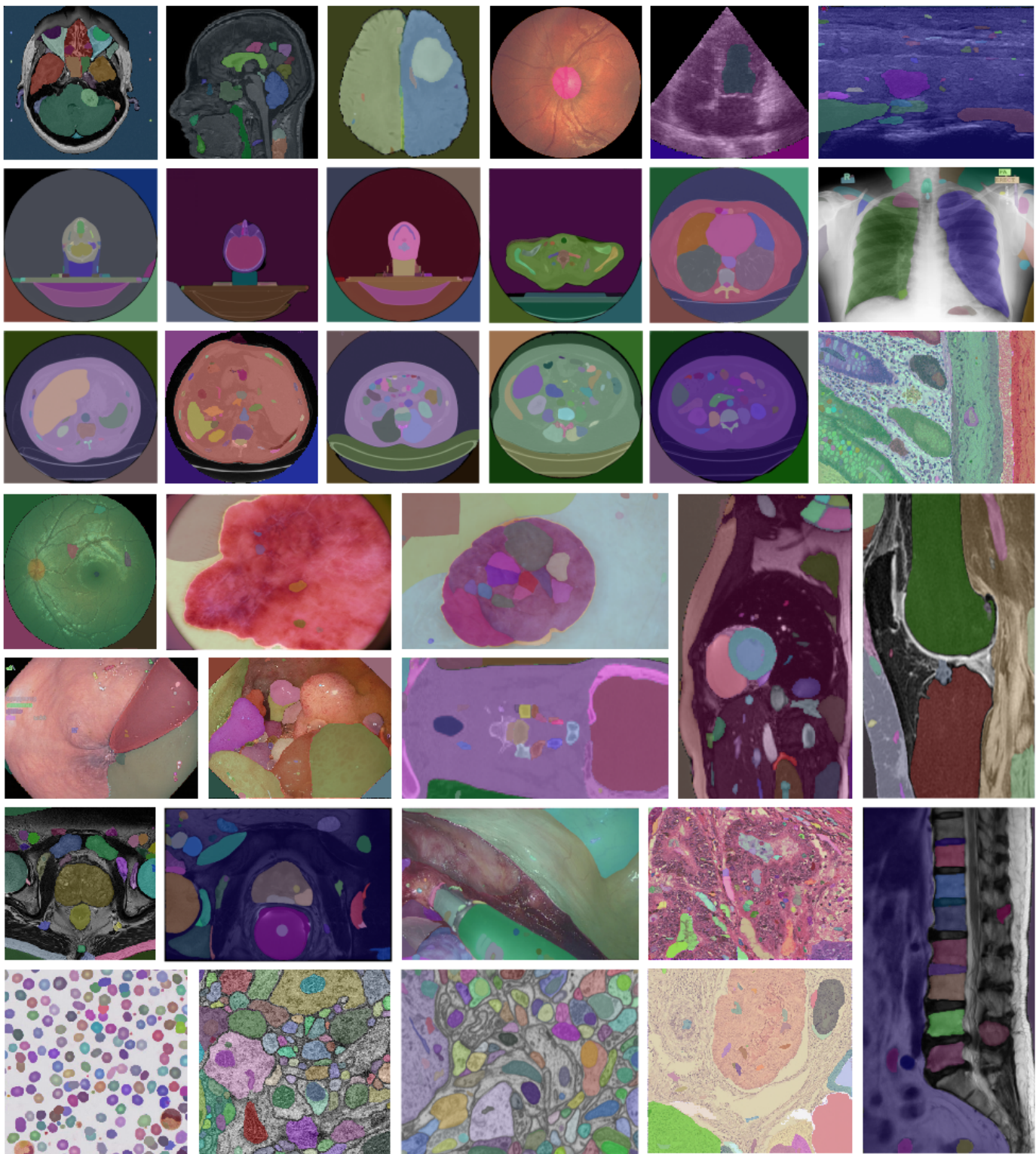


Fig. 9. Visualization results of the *everything* mode with *ViT-H*.

F. Ablation Study on the Number of Points in Everything Mode

As described above, in the *everything* mode, a grid of points prompts ($m \times m$) will be generated. In default, m is set to 32. Obviously, the number of points will have an impact on the final segmentation performance. Especially for images that have multiple targets with different sizes, improper parameter

designs will lead to imperfect segmentation with some objects being unprompted. As shown in Table XI, we tested four datasets with multiple objects on one image. The results show that in these four datasets, as the number of points increases from 8^2 to 256^2 , the DICE also increases gradually. It can also be observed from Fig. 10 that more points will bring

more potential objects (shown in different colors). Besides, too many points make SAM tend to split an object into several pieces, thus destroying the integrity of the object. Moreover, increasing the number of points can also lead to a significant increase in test time. Hence, it is a trade-off between the segmentation performance and test efficiency.

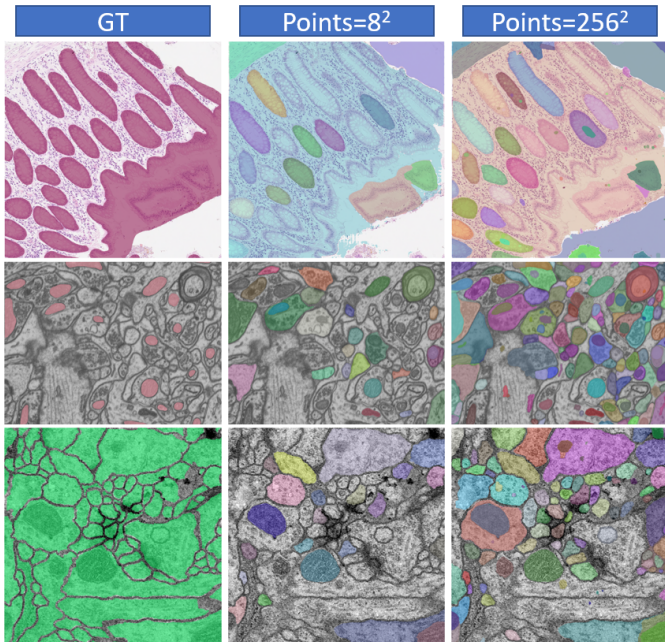


Fig. 10. Different cases of O_4 [79], O_5 [38] and O_6 [73] with different numbers of points in S_{1H} .

TABLE XII
SPEARMAN'S RANK CORRELATION COEFFICIENT. ($p < 0.001$)

	S_{1B}	S_{1H}	S_2	S_3	S_4	S_5	S_6
Size	0.400	0.491	0.467	0.563	0.470	0.520	0.541
Aspect Ratio	0.062	0.0435	0.0868	0.060	0.058	0.068	0.072
Intensity Difference	0.372	0.433	0.365	0.327	0.321	0.265	0.280
Fourier Order	-0.347	-0.410	-0.491	-0.649	-0.582	-0.607	-0.652

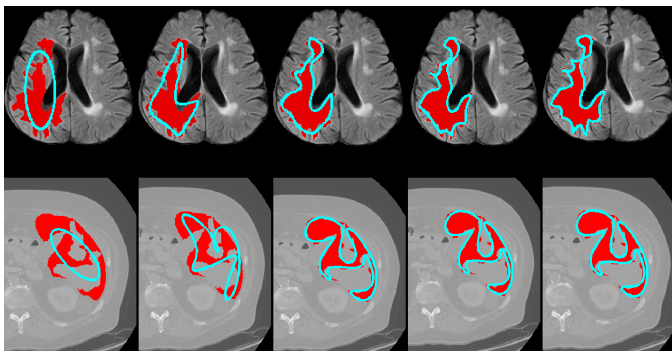


Fig. 11. Contour decoded from the Fourier series. From left to right, decoded contour (blue) gets closer to the original contours (red) as the FO increases.

G. Analysis of Factors Correlating to Segmentation Results

To verify which factors affect the segmentation performance of SAM, we recorded the size, aspect ratio, intensity difference

between foreground and background, and boundary complexity of 195100 anatomical structures. By analyzing these factors, we aim to better understand the correlation between anatomical structure characteristics and SAM's segmentation performance, and further provide some useful insights into the development of medical SAM.

The size of the anatomical structure was computed as the pixel-level area of the corresponding mask. To determine the aspect ratio of a mask, the ratio between the shorter and longer sides (0-1) of its bounding box needs to be computed. The intensity difference was defined as the difference in the mean intensity value between the structure and the rest of the area within the enlarged bounding box except for the structure. Specifically, due to the wide-range dimensions of targets, we extend the box adaptively outward by a preset ratio (0.1) instead of setting fixed enlarged pixel values (e.g., extend 10 pixels). Additionally, we introduced Elliptical Fourier Descriptors (EFD) [90] to describe boundary complexity.

EFD encodes the contour of a mask into a Fourier series that represents different frequency components. As the Fourier order (FO) increases, the contour decoded from the Fourier series gets closer to the original contour (see Fig. 11), and the decoding process can be described as Eq. 3.

$$\begin{aligned} x_N(t) &= L_x + \sum_{n=1}^N (a_n \sin(\frac{T}{2n\pi t}) + b_n \cos(\frac{T}{2n\pi t})) \\ y_N(t) &= L_y + \sum_{n=1}^N (c_n \sin(\frac{T}{2n\pi t}) + d_n \cos(\frac{T}{2n\pi t})) \end{aligned} \quad (3)$$

where $(x_N(t), y_N(t))$ is the coordinates of any point on the contour, N is the number of Fourier series expansions, and $t \in [0, T]$ denotes the different sampling locations. (L_x, L_y) indicates the coordinates of the contour's center point, (a_n, b_n) denotes the parameter obtained by Fourier coding of the x-coordinates, and (c_n, d_n) denotes the encoding result in the y-direction. We can roughly estimate the complexity of the object boundary in terms of the FO. Specifically, the order is defined as the required number of accumulations when the contour from decoded Fourier series reaches a certain degree of overlap (we use DICE to represent overlap) with the original contour. However, when using this approach as a quantitative measure, it is especially important to set an appropriate DICE threshold. A low threshold will not be able to accurately distinguish the difference in complexity among various object boundaries. Meanwhile, if the threshold is too high, the EFD may fail in fitting the complex contours as required and get into an infinite calculation. Thus, we optimized the representation of FO to avoid the EFD program from getting stuck in endless accumulation (see cumulative terms in Eq. 3). For different structures, we increased the FO from 1 and calculated the DICE between the decoded contour and the original contour at each step. Then we set two ways to end the process: 1) $DICE > 97.0\%$; 2) the difference in the DICE between order $F_{(a-1)}$ and order $F_{(a)}$ is less than 0.1%. Consequently, we record the FO ($F_{(a)}$) and DICE after termination. Finally, we take $F_{final} = F_a + n \times 100 \times (1 - DICE)$, $n = 2$ as the final optimized FO.

We analyzed the correlation between the above four attributes of the target objects and the DICE using Spearman's

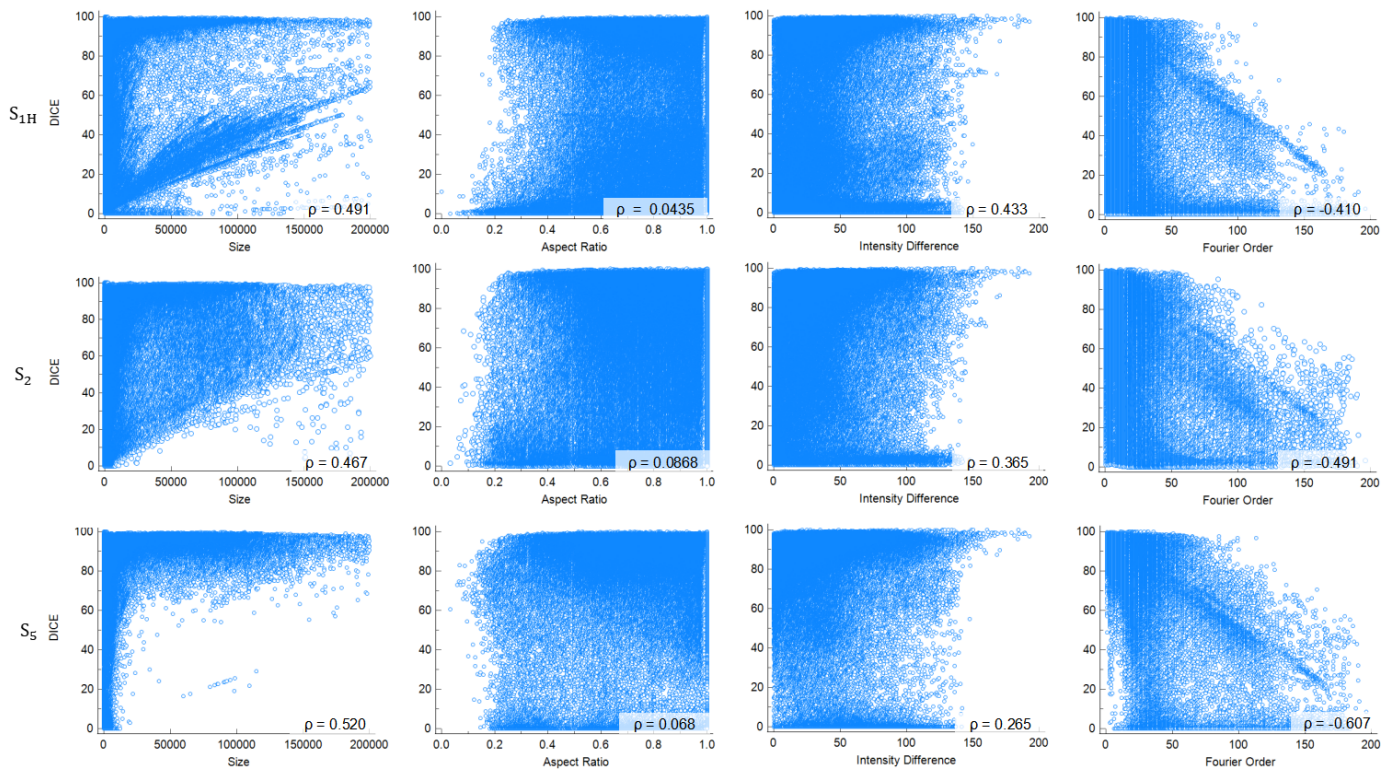


Fig. 12. Scatterplot of different object attributes with DICE.

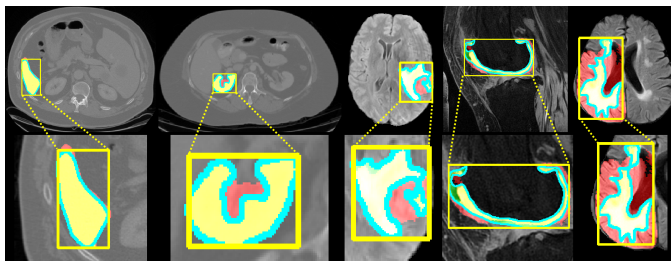


Fig. 13. Relationship between DICE and FO. From left to right, FO gradually increases. The yellow box represents the box prompt, the red mask is the prediction, the green mask is the GT, the yellow mask is the overlap of prediction and GT, and the blue contour is decoded from the Fourier series.

rank correlation coefficient under different testing strategies. Results are shown in Table XII and Fig. 12. Under most testing strategies, the DICE score was found to have a medium correlation ($0.4 \leq \rho < 0.7$) with the size and FO, a weak correlation ($0.2 \leq \rho < 0.4$) with the intensity difference, and no correlation with the aspect ratio. In other words, SAM can robustly segment medical targets with different aspect ratios. However, the segmentation performance tends to be poor when segmenting objects with small sizes, complex boundaries, or low contrast. As shown in Fig. 13, under S_5 , the DICE decreases as the FO increases. Additionally, to verify the influence of boundary complexity on SAM's segmentation ability, we analyzed the correlation between FO and DICE when the object's size had no or weak correlation with DICE. Taking S_5 as an example, we selected a total of 96,728 anatomical structures with a size in the range

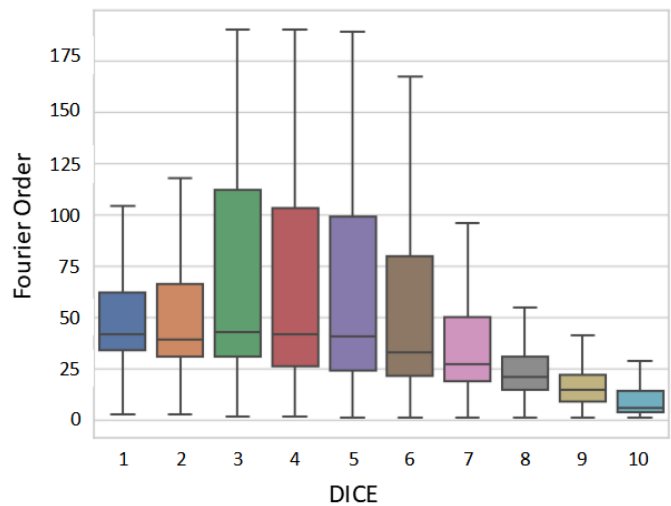


Fig. 14. FO boxplot of different DICE ranges under low correlation of Size.

[1000,10000]. The correlation coefficient between the DICE and the structure's size was 0.141 ($p < 0.001$), and with FO is -0.542 ($p < 0.001$). Moreover, we divided DICE into ten levels on average (e.g., level-1 means DICE (%) belongs to (0,10]) and visualized the FO boxplot of different DICE levels in Fig. 14. The results show that the FO distribution of the structure gradually shifts to a range with smaller values as the DICE level increases. This means that shape/boundary complexity may affect SAM's segmentation performance, regardless of the size of the objects.

V. DISCUSSION AND CONCLUSION

In this study, we comprehensively evaluated the SAM for the segmentation of a large medical dataset. Based on the aforementioned empirical analyses, our conclusions are as follows: 1) *Everything* mode is not suitable for most medical images. In this mode, SAM shows poor perception of medical objects. Therefore, this causes SAM to output a lot of false-positive masks and perform unstable with high standard deviations. 2) Setting different numbers of point prompts in automatic *everything* mode will greatly influence the segmentation performance. It is a trade-off between segmentation performance and testing efficiency. 3) In the *prompt* mode, after adding the manual hints, SAM gets more information about the object. Therefore, its segmentation performance is also improved. 4) Adding more positive points can significantly improve SAM's segmentation results. However, the inclusion of negative points needs to be very careful, because the foreground and background in medical images could be easily confused. 5) The box prompt contains rich position information on the object's position. Hence, it performed better in most medical segmentation tasks in our study, compared to the point prompts. 6) The hybrid of point and box prompts showed no improvement on the tasks in the current study. This may be related to SAM's ability to encode mixed prompts. 7) The performance of SAM in different modalities/objects is quite different, even for different modalities of the same object, highlighting its instability. This proves that SAM cannot stably and accurately implement zero-shot segmentation on multi-modal and multi-object medical datasets. 8) Different attributes of the medical objects may affect SAM's object perception ability. In particular, SAM may output poor results for objects with complex shapes/boundaries, small sizes, or low contrast. Finally, we believe that although SAM has the potential to become a general MIS model, its performance in the MIS task is not stable at present. Hence, future research should investigate how to efficiently use few medical images to finetune SAM to improve its reliability. Additionally, it is also an interesting direction to explore SAM's segmentation performance for 3D volume data. We hope that this report will help readers and the community better understand SAM's segmentation performance in medical images, and ultimately facilitate the development of a new generation of MIS foundation models.

VI. ACKNOWLEDGEMENT

The authors of this paper sincerely appreciate all the challenge organizers and owners for providing the public MIS datasets including AbdomenCT-1K, ACDC, AMOS 2022, AutoLaparo, BrainPTM 2021, BraTS20, CAMUS, CHAOS, CHASE-DB1, Chest CT segmentation, CRAG, crossMoDA, CVC-ClinicDB, DRIVE, EndoTect 2020, EPFL-EM, ETIS-Larib Polyp DB, FeTA, HaN-Seg, I2CVB, iChallenge-AMD, iChallenge-PALM, IDR 2018, iSeg 2019, ISIC 2018, IXI, KiPA22, KiTS19, KiTS21, Kvasir-Instrumen, Kvasir-SEG, LiVScar, LUNA16, M&Ms, MALBCV-Abdomen, Montgomery County CXR Set, MRSpineSeg, MSD, NCI-ISBI 2013, NeurIPS 2022, PROMISE12, QUBIQ

2021, SIIM-ACR, SKI10, SLIVER07, ssTEM, STARE, TN-SCUI, VerSe19&VerSe20, Warwick-QU, WORD, and 4C2021 C04 TLS01. We also thank Meta AI for releasing the source code of SAM publicly available.

REFERENCES

- [1] A. Radford, J. W. Kim, C. Hallacy, A. Ramesh, G. Goh, S. Agarwal, G. Sastry, A. Askell, P. Mishkin, J. Clark *et al.*, "Learning transferable visual models from natural language supervision," in *International conference on machine learning*. PMLR, 2021, pp. 8748–8763.
- [2] C. Jia, Y. Yang, Y. Xia, Y.-T. Chen, Z. Parekh, H. Pham, Q. Le, Y.-H. Sung, Z. Li, and T. Duerig, "Scaling up visual and vision-language representation learning with noisy text supervision," in *International Conference on Machine Learning*. PMLR, 2021, pp. 4904–4916.
- [3] A. Ramesh, M. Pavlov, G. Goh, S. Gray, C. Voss, A. Radford, M. Chen, and I. Sutskever, "Zero-shot text-to-image generation," in *International Conference on Machine Learning*. PMLR, 2021, pp. 8821–8831.
- [4] A. Kirillov, E. Mintun, N. Ravi, H. Mao, C. Rolland, L. Gustafson, T. Xiao, S. Whitehead, A. C. Berg, W.-Y. Lo *et al.*, "Segment anything," *arXiv preprint arXiv:2304.02643*, 2023.
- [5] A. Dosovitskiy, L. Beyer, A. Kolesnikov, D. Weissenborn, X. Zhai, T. Unterthiner, M. Dehghani, M. Minderer, G. Heigold, S. Gelly *et al.*, "An image is worth 16x16 words: Transformers for image recognition at scale," in *International Conference on Learning Representations*.
- [6] L. Tang, H. Xiao, and B. Li, "Can sam segment anything? when sam meets camouflaged object detection," *arXiv preprint arXiv:2304.04709*, 2023.
- [7] G.-P. Ji, D.-P. Fan, P. Xu, M.-M. Cheng, B. Zhou, and L. Van Gool, "Sam struggles in concealed scenes—empirical study on" segment anything"," *arXiv preprint arXiv:2304.06022*, 2023.
- [8] W. Ji, J. Li, Q. Bi, W. Li, and L. Cheng, "Segment anything is not always perfect: An investigation of sam on different real-world applications," *arXiv preprint arXiv:2304.05750*, 2023.
- [9] S. Mohapatra, A. Gosai, and G. Schlaug, "Brain extraction comparing segment anything model (sam) and fsl brain extraction tool," *arXiv preprint arXiv:2304.04738*, 2023.
- [10] R. Deng, C. Cui, Q. Liu, T. Yao, L. W. Remedios, S. Bao, B. A. Landman, L. E. Wheless, L. A. Coburn, K. T. Wilson *et al.*, "Segment anything model (sam) for digital pathology: Assess zero-shot segmentation on whole slide imaging," *arXiv preprint arXiv:2304.04155*, 2023.
- [11] T. Zhou, Y. Zhang, Y. Zhou, Y. Wu, and C. Gong, "Can sam segment polyps?" *arXiv preprint arXiv:2304.07583*, 2023.
- [12] S. Pieper, M. Halle, and R. Kikinis, "3d slicer," in *2004 2nd IEEE international symposium on biomedical imaging: nano to macro (IEEE Cat No. 04EX821)*. IEEE, 2004, pp. 632–635.
- [13] Y. Liu, J. Zhang, Z. She, A. Kheradmand, and M. Armand, "Samm (segment any medical model): A 3d slicer integration to sam," *arXiv preprint arXiv:2304.05622*, 2023.
- [14] S. He, R. Bao, J. Li, P. E. Grant, and Y. Ou, "Accuracy of segment-anything model (sam) in medical image segmentation tasks," *arXiv preprint arXiv:2304.09324*, 2023.
- [15] M. A. Mazurowski, H. Dong, H. Gu, J. Yang, N. Konz, and Y. Zhang, "Segment anything model for medical image analysis: an experimental study," 2023.
- [16] J. Ma and B. Wang, "Segment anything in medical images," 2023.
- [17] J. Wu, R. Fu, H. Fang, Y. Liu, Z. Wang, Y. Xu, Y. Jin, and T. Arbel, "Medical sam adapter: Adapting segment anything model for medical image segmentation," 2023.
- [18] F. Isensee, P. F. Jaeger, S. A. Kohl, J. Petersen, and K. H. Maier-Hein, "nnu-net: a self-configuring method for deep learning-based biomedical image segmentation," *Nature methods*, vol. 18, no. 2, pp. 203–211, 2021.
- [19] E. K. Wang, C.-M. Chen, M. M. Hassan, and A. Almogren, "A deep learning based medical image segmentation technique in internet-of-medical-things domain," *Future Generation Computer Systems*, vol. 108, pp. 135–144, 2020.
- [20] V. I. Butoi, J. J. G. Ortiz, T. Ma, M. R. Sabuncu, J. Guttag, and A. V. Dalca, "Universeg: Universal medical image segmentation," *arXiv preprint arXiv:2304.06131*, 2023.
- [21] J. Ma, Y. Zhang, S. Gu, C. Zhu, C. Ge, Y. Zhang, X. An, C. Wang, Q. Wang, X. Liu, S. Cao, Q. Zhang, S. Liu, Y. Wang, Y. Li, J. He, and X. Yang, "Abdomenct-1k: Is abdominal organ segmentation a solved problem?" *IEEE Transactions on Pattern Analysis and Machine Intelligence*, vol. 44, no. 10, pp. 6695–6714, 2022.

- [22] O. Bernard, A. Lalande, C. Zotti, F. Cervenansky, X. Yang, P.-A. Heng, I. Cetin, K. Lekadir, O. Camara, M. A. G. Ballester *et al.*, “Deep learning techniques for automatic mri cardiac multi-structures segmentation and diagnosis: is the problem solved?” *IEEE transactions on medical imaging*, vol. 37, no. 11, pp. 2514–2525, 2018.
- [23] Y. Ji, H. Bai, J. Yang, C. Ge, Y. Zhu, R. Zhang, Z. Li, L. Zhang, W. Ma, X. Wan *et al.*, “Amos: A large-scale abdominal multi-organ benchmark for versatile medical image segmentation,” *arXiv preprint arXiv:2206.08023*, 2022.
- [24] Z. Wang, B. Lu, Y. Long, F. Zhong, T.-H. Cheung, Q. Dou, and Y. Liu, “Autolapar: A new dataset of integrated multi-tasks for image-guided surgical automation in laparoscopic hysterectomy,” 2022.
- [25] I. Avital, I. Nelkenbaum, G. Tsarfaty, E. Konen, N. Kiryati, and A. Mayer, “Neural segmentation of seeding rois (srois) for pre-surgical brain tractography,” *IEEE transactions on medical imaging*, vol. 39, no. 5, pp. 1655–1667, 2019.
- [26] B. H. Menze, A. Jakab, S. Bauer, J. Kalpathy-Cramer, K. Farahani, J. Kirby, Y. Burren, N. Porz, J. Slotboom, R. Wiest *et al.*, “The multimodal brain tumor image segmentation benchmark (brats),” *IEEE transactions on medical imaging*, vol. 34, no. 10, pp. 1993–2024, 2014.
- [27] S. Bakas, H. Akbari, A. Sotiras, M. Bilello, M. Rozycki, J. S. Kirby, J. B. Freymann, K. Farahani, and C. Davatzikos, “Advancing the cancer genome atlas glioma mri collections with expert segmentation labels and radiomic features,” *Scientific data*, vol. 4, no. 1, pp. 1–13, 2017.
- [28] S. Bakas, M. Reyes, A. Jakab, S. Bauer, M. Rempfler, A. Crimi, R. T. Shinohara, C. Berger, S. M. Ha, M. Rozycki *et al.*, “Identifying the best machine learning algorithms for brain tumor segmentation, progression assessment, and overall survival prediction in the brats challenge,” *arXiv preprint arXiv:1811.02629*, 2018.
- [29] S. Leclerc, E. Smistad, J. Pedrosa, A. Østvik, F. Cervenansky, F. Espinosa, T. Espeland, E. A. R. Berg, P.-M. Jodoin, T. Grenier *et al.*, “Deep learning for segmentation using an open large-scale dataset in 2d echocardiography,” *IEEE transactions on medical imaging*, vol. 38, no. 9, pp. 2198–2210, 2019.
- [30] A. E. Kavur, N. S. Gezer, M. Barış, S. Aslan, P.-H. Conze, V. Groza, D. D. Pham, S. Chatterjee, P. Ernst, S. Özkan *et al.*, “Chaos challenge-combined (ct-mr) healthy abdominal organ segmentation,” *Medical Image Analysis*, vol. 69, p. 101950, 2021.
- [31] J. Zhang, B. Dashtbozorg, E. Bekkers, J. P. Pluim, R. Duits, and B. M. ter Haar Romeny, “Robust retinal vessel segmentation via locally adaptive derivative frames in orientation scores,” *IEEE transactions on medical imaging*, vol. 35, no. 12, pp. 2631–2644, 2016.
- [32] “Chest CT Segmentation Dataset,” [EB/OL], <https://www.kaggle.com/datasets/polomarco/chest-ct-segmentation>.
- [33] S. Graham, H. Chen, J. Gamper, Q. Dou, P.-A. Heng, D. Snead, Y. W. Tsang, and N. Rajpoot, “Mild-net: Minimal information loss dilated network for gland instance segmentation in colon histology images,” *Medical image analysis*, vol. 52, pp. 199–211, 2019.
- [34] J. Shapey, G. Wang, R. Dorent, A. Dimitriadis, W. Li, I. Paddick, N. Kitchen, S. Bisdas, S. R. Saeed, S. Ourselin *et al.*, “An artificial intelligence framework for automatic segmentation and volumetry of vestibular schwannomas from contrast-enhanced t1-weighted and high-resolution t2-weighted mri,” *Journal of neurosurgery*, vol. 134, no. 1, pp. 171–179, 2019.
- [35] J. Bernal, F. J. Sánchez, G. Fernández-Esparrach, D. Gil, C. Rodríguez, and F. Vilarinho, “Wm-dova maps for accurate polyp highlighting in colonoscopy: Validation vs. saliency maps from physicians,” *Computerized medical imaging and graphics*, vol. 43, pp. 99–111, 2015.
- [36] W. Liu, H. Yang, T. Tian, Z. Cao, X. Pan, W. Xu, Y. Jin, and F. Gao, “Full-resolution network and dual-threshold iteration for retinal vessel and coronary angiograph segmentation,” *IEEE Journal of Biomedical and Health Informatics*, vol. 26, no. 9, pp. 4623–4634, 2022.
- [37] S. A. Hicks, D. Jha, V. Thambawita, P. Halvorsen, H. L. Hammer, and M. A. Riegler, “The endotect 2020 challenge: evaluation and comparison of classification, segmentation and inference time for endoscopy,” in *Pattern Recognition. ICPR International Workshops and Challenges: Virtual Event, January 10-15, 2021, Proceedings, Part VIII*. Springer, 2021, pp. 263–274.
- [38] A. Lucchi, Y. Li, and P. Fua, “Learning for structured prediction using approximate subgradient descent with working sets,” in *Proceedings of the IEEE Conference on Computer Vision and Pattern Recognition*, 2013, pp. 1987–1994.
- [39] D. Yoon, H.-J. Kong, B. S. Kim, W. S. Cho, J. C. Lee, M. Cho, M. H. Lim, S. Y. Yang, S. H. Lim, J. Lee *et al.*, “Colonoscopic image synthesis with generative adversarial network for enhanced detection of sessile serrated lesions using convolutional neural network,” *Scientific reports*, vol. 12, no. 1, p. 261, 2022.
- [40] K. Payette, P. de Dumast, H. Kebiri, I. Ezhov, J. C. Paetzold, S. Shit, A. Iqbal, R. Khan, R. Kottke, P. Grethen *et al.*, “An automatic multi-tissue human fetal brain segmentation benchmark using the fetal tissue annotation dataset,” *Scientific Data*, vol. 8, no. 1, p. 167, 2021.
- [41] G. Podobnik, P. Strojani, P. Peterlin, B. Ibragimov, and T. Vrtovec, “Hanseg: The head and neck organ-at-risk ct & mr segmentation dataset,” *Medical Physics*, 2023.
- [42] G. Lemaitre, R. Martí, J. Freixenet, J. C. Vilanova, P. M. Walker, and F. Meriaudeau, “Computer-aided detection and diagnosis for prostate cancer based on mono and multi-parametric mri: a review,” *Computers in biology and medicine*, vol. 60, pp. 8–31, 2015.
- [43] X. Li, M. Jia, M. T. Islam, L. Yu, and L. Xing, “Self-supervised feature learning via exploiting multi-modal data for retinal disease diagnosis,” *IEEE Transactions on Medical Imaging*, vol. 39, no. 12, pp. 4023–4033, 2020.
- [44] F. Huazhu, L. Fei, and I. José, “Palm: Pathologic myopia challenge,” *Comput. Vis. Med. Imaging*, 2019.
- [45] P. Porwal, S. Pachade, R. Kamble, M. Kokare, G. Deshmukh, V. Sahasrabudhe, and F. Meriaudeau, “Indian diabetic retinopathy image dataset (idrid): a database for diabetic retinopathy screening research,” *Data*, vol. 3, no. 3, p. 25, 2018.
- [46] Y. Sun, K. Gao, Z. Wu, G. Li, X. Zong, Z. Lei, Y. Wei, J. Ma, X. Yang, X. Feng *et al.*, “Multi-site infant brain segmentation algorithms: the iseg-2019 challenge,” *IEEE Transactions on Medical Imaging*, vol. 40, no. 5, pp. 1363–1376, 2021.
- [47] P. Tschandl, C. Rosendahl, and H. Kittler, “The ham10000 dataset, a large collection of multi-source dermatoscopic images of common pigmented skin lesions,” *Scientific data*, vol. 5, no. 1, pp. 1–9, 2018.
- [48] N. C. Codella, D. Gutman, M. E. Celebi, B. Helba, M. A. Marchetti, S. W. Dusza, A. Kalloo, K. Liopyris, N. Mishra, H. Kittler *et al.*, “Skin lesion analysis toward melanoma detection: A challenge at the 2017 international symposium on biomedical imaging (isbi), hosted by the international skin imaging collaboration (isic),” in *2018 IEEE 15th international symposium on biomedical imaging (ISBI 2018)*. IEEE, 2018, pp. 168–172.
- [49] N. Codella, V. Rotemberg, P. Tschandl, M. E. Celebi, S. Dusza, D. Gutman, B. Helba, A. Kalloo, K. Liopyris, M. Marchetti *et al.*, “Skin lesion analysis toward melanoma detection 2018: A challenge hosted by the international skin imaging collaboration (isic),” *arXiv preprint arXiv:1902.03368*, 2019.
- [50] “IXI Dataset,” [EB/OL], <https://brain-development.org/ixi-dataset/>.
- [51] Y. He, G. Yang, J. Yang, R. Ge, Y. Kong, X. Zhu, S. Zhang, P. Shao, H. Shu, J.-L. Dillenseger *et al.*, “Meta grayscale adaptive network for 3d integrated renal structures segmentation,” *Medical image analysis*, vol. 71, p. 102055, 2021.
- [52] Y. He, G. Yang, J. Yang, Y. Chen, Y. Kong, J. Wu, L. Tang, X. Zhu, J.-L. Dillenseger, P. Shao *et al.*, “Dense biased networks with deep priori anatomy and hard region adaptation: Semi-supervised learning for fine renal artery segmentation,” *Medical image analysis*, vol. 63, p. 101722, 2020.
- [53] P. Shao, C. Qin, C. Yin, X. Meng, X. Ju, J. Li, Q. Lv, W. Zhang, and Z. Xu, “Laparoscopic partial nephrectomy with segmental renal artery clamping: technique and clinical outcomes,” *European urology*, vol. 59, no. 5, pp. 849–855, 2011.
- [54] P. Shao, L. Tang, P. Li, Y. Xu, C. Qin, Q. Cao, X. Ju, X. Meng, Q. Lv, J. Li *et al.*, “Precise segmental renal artery clamping under the guidance of dual-source computed tomography angiography during laparoscopic partial nephrectomy,” *European urology*, vol. 62, no. 6, pp. 1001–1008, 2012.
- [55] N. Heller, N. Sathianathen, A. Kalapara, E. Walczak, K. Moore, H. Kaluzniak, J. Rosenberg, P. Blake, Z. Rengel, M. Oestreich, J. Dean, M. Tradewell, A. Shah, R. Tejjpaul, Z. Edgerton, M. Peterson, S. Raza, S. Regmi, N. Papanikolopoulos, and C. Weight, “The kits19 challenge data: 300 kidney tumor cases with clinical context, ct semantic segmentations, and surgical outcomes,” 2020.
- [56] Z. Zhao, H. Chen, and L. Wang, “A coarse-to-fine framework for the 2021 kidney and kidney tumor segmentation challenge,” in *Kidney and Kidney Tumor Segmentation: MICCAI 2021 Challenge, KiTS 2021, Held in Conjunction with MICCAI 2021, Strasbourg, France, September 27, 2021, Proceedings*. Springer, 2022, pp. 53–58.
- [57] D. Jha, S. Ali, K. Emanuelsen, S. A. Hicks, V. Thambawita, E. Garcia-Ceja, M. A. Riegler, T. de Lange, P. T. Schmidt, H. D. Johansen, D. Johansen, and P. Halvorsen, “Kvasir-instrument: Diagnostic and therapeutic tool segmentation dataset in gastrointestinal endoscopy,” in *MultiMedia Modeling*. Cham: Springer International Publishing, 2021, pp. 218–229.

- [58] D. Jha, P. H. Smedsrud, M. A. Riegler, P. Halvorsen, T. de Lange, D. Johansen, and H. D. Johansen, "Kvasir-seg: A segmented polyp dataset," in *International Conference on Multimedia Modeling*. Springer, 2020, pp. 451–462.
- [59] R. Karim, P. Bhagirath, P. Claus, R. J. Housden, Z. Chen, Z. Karimghaloo, H.-M. Sohn, L. L. Rodríguez, S. Vera, X. Albà *et al.*, "Evaluation of state-of-the-art segmentation algorithms for left ventricle infarct from late gadolinium enhancement mr images," *Medical image analysis*, vol. 30, pp. 95–107, 2016.
- [60] A. A. A. Setio, A. Traverso, T. De Bel, M. S. Berens, C. Van Den Bogaard, P. Cerello, H. Chen, Q. Dou, M. E. Fantacci, B. Geurts *et al.*, "Validation, comparison, and combination of algorithms for automatic detection of pulmonary nodules in computed tomography images: the luna16 challenge," *Medical image analysis*, vol. 42, pp. 1–13, 2017.
- [61] V. M. Campello, P. Gkontra, C. Izquierdo, C. Martin-Isla, A. Sojoudi, P. M. Full, K. Maier-Hein, Y. Zhang, Z. He, J. Ma *et al.*, "Multi-centre, multi-vendor and multi-disease cardiac segmentation: the m&ms challenge," *IEEE Transactions on Medical Imaging*, vol. 40, no. 12, pp. 3543–3554, 2021.
- [62] Y. Zhou, Z. Li, S. Bai, C. Wang, X. Chen, M. Han, E. Fishman, and A. L. Yuille, "Prior-aware neural network for partially-supervised multi-organ segmentation," in *Proceedings of the IEEE/CVF international conference on computer vision*, 2019, pp. 10 672–10 681.
- [63] S. Jaeger, S. Candemir, S. Antani, Y.-X. J. Wáng, P.-X. Lu, and G. Thoma, "Two public chest x-ray datasets for computer-aided screening of pulmonary diseases," *Quantitative imaging in medicine and surgery*, vol. 4, no. 6, p. 475, 2014.
- [64] S. Pang, C. Pang, L. Zhao, Y. Chen, Z. Su, Y. Zhou, M. Huang, W. Yang, H. Lu, and Q. Feng, "Spineparsenet: spine parsing for volumetric mr image by a two-stage segmentation framework with semantic image representation," *IEEE Transactions on Medical Imaging*, vol. 40, no. 1, pp. 262–273, 2020.
- [65] A. L. Simpson, M. Antonelli, S. Bakas, M. Bilello, K. Farahani, B. Van Ginneken, A. Kopp-Schneider, B. A. Landman, G. Litjens, B. Menze *et al.*, "A large annotated medical image dataset for the development and evaluation of segmentation algorithms," *arXiv preprint arXiv:1902.09063*, 2019.
- [66] A. Li, C. Li, X. Wang, S. Eberl, D. D. Feng, and M. Fulham, "Automated segmentation of prostate mr images using prior knowledge enhanced random walker," in *2013 International Conference on Digital Image Computing: Techniques and Applications (DICTA)*. IEEE, 2013, pp. 1–7.
- [67] G. Lee, S. Kim, J. Kim, and S.-Y. Yun, "Mediar: Harmony of data-centric and model-centric for multi-modality microscopy," 2022.
- [68] G. Litjens, R. Toth, W. Van De Ven, C. Hoeks, S. Kerkstra, B. van Ginneken, G. Vincent, G. Guillard, N. Birbeck, J. Zhang *et al.*, "Evaluation of prostate segmentation algorithms for mri: the promise12 challenge," *Medical image analysis*, vol. 18, no. 2, pp. 359–373, 2014.
- [69] W. Ji, S. Yu, J. Wu, K. Ma, C. Bian, Q. Bi, J. Li, H. Liu, L. Cheng, and Y. Zheng, "Learning calibrated medical image segmentation via multi-rater agreement modeling," in *Proceedings of the IEEE/CVF Conference on Computer Vision and Pattern Recognition*, 2021, pp. 12 341–12 351.
- [70] O. Viniavskiy, M. Dobko, and O. Doboševych, "Weakly-supervised segmentation for disease localization in chest x-ray images," in *Artificial Intelligence in Medicine: 18th International Conference on Artificial Intelligence in Medicine, AIME 2020, Minneapolis, MN, USA, August 25–28, 2020, Proceedings 18*. Springer, 2020, pp. 249–259.
- [71] S. Lee, H. Shim, S. H. Park, I. D. Yun, and S. U. Lee, "Learning local shape and appearance for segmentation of knee cartilage in 3d mri," in *Medical Image Analysis for the Clinic: a Grand Challenge. In Proceedings of the 13th International Conference on Medical Image Computing and Computer Assisted Intervention (MICCAI 2010), Beijing, China, 2010*, pp. 231–240.
- [72] T. Heimann, B. Van Ginneken, M. A. Styner, Y. Arzhaeva, V. Aurich, C. Bauer, A. Beck, C. Becker, R. Beichel, G. Bekes *et al.*, "Comparison and evaluation of methods for liver segmentation from ct datasets," *IEEE transactions on medical imaging*, vol. 28, no. 8, pp. 1251–1265, 2009.
- [73] A. Cardona, S. Saalfeld, S. Preibisch, B. Schmid, A. Cheng, J. Pulokas, P. Tomancak, and V. Hartenstein, "An integrated micro-and macroarchitectural analysis of the drosophila brain by computer-assisted serial section electron microscopy," *PLoS biology*, vol. 8, no. 10, p. e1000502, 2010.
- [74] A. Hoover, V. Kouznetsova, and M. Goldbaum, "Locating blood vessels in retinal images by piecewise threshold probing of a matched filter response," *IEEE Transactions on Medical imaging*, vol. 19, no. 3, pp. 203–210, 2000.
- [75] Q. Kang, Q. Lao, Y. Li, Z. Jiang, Y. Qiu, S. Zhang, and K. Li, "Thyroid nodule segmentation and classification in ultrasound images through intra-and inter-task consistent learning," *Medical image analysis*, vol. 79, p. 102443, 2022.
- [76] A. Sekuboyina, M. E. Husseini, A. Bayat, M. Löffler, H. Liebl, H. Li, G. Tetteh, J. Kukačka, C. Payer, D. Stern *et al.*, "Verse: A vertebrae labelling and segmentation benchmark for multi-detector ct images," *Medical image analysis*, vol. 73, p. 102166, 2021.
- [77] M. T. Löffler, A. Sekuboyina, A. Jacob, A.-L. Grau, A. Scharr, M. El Husseini, M. Kallweit, C. Zimmer, T. Baum, and J. S. Kirschke, "A vertebral segmentation dataset with fracture grading," *Radiology: Artificial Intelligence*, vol. 2, no. 4, p. e190138, 2020.
- [78] H. Liebl, D. Schinz, A. Sekuboyina, L. Malagutti, M. T. Löffler, A. Bayat, M. El Husseini, G. Tetteh, K. Grau, E. Niederreiter *et al.*, "A computed tomography vertebral segmentation dataset with anatomical variations and multi-vendor scanner data," *Scientific Data*, vol. 8, no. 1, p. 284, 2021.
- [79] K. Sirinukunwattana, J. P. Pluim, H. Chen, X. Qi, P.-A. Heng, Y. B. Guo, L. Y. Wang, B. J. Matuszewski, E. Bruni, U. Sanchez *et al.*, "Gland segmentation in colon histology images: The glas challenge contest," *Medical image analysis*, vol. 35, pp. 489–502, 2017.
- [80] X. Luo, W. Liao, J. Xiao, J. Chen, T. Song, X. Zhang, K. Li, D. N. Metaxas, G. Wang, and S. Zhang, "Word: A large scale dataset, benchmark and clinical applicable study for abdominal organ segmentation from ct image," *Medical Image Analysis*, vol. 82, p. 102642, 2022.
- [81] "4C2021 C04 TLS01 Dataset." [EB/OL], <https://aistudio.baidu.com/aistudio/projectdetail/1952488?channelType=1&channel=1>.
- [82] J. Liang, X. Yang, Y. Huang, H. Li, S. He, X. Hu, Z. Chen, W. Xue, J. Cheng, and D. Ni, "Sketch guided and progressive growing gan for realistic and editable ultrasound image synthesis," *Medical Image Analysis*, vol. 79, p. 102461, 2022.
- [83] K. He, X. Chen, S. Xie, Y. Li, P. Dollár, and R. Girshick, "Masked autoencoders are scalable vision learners," in *Proceedings of the IEEE/CVF Conference on Computer Vision and Pattern Recognition*, 2022, pp. 16 000–16 009.
- [84] M. Tancik, P. Srinivasan, B. Mildenhall, S. Fridovich-Keil, N. Raghavan, U. Singhal, R. Ramamoorthi, J. Barron, and R. Ng, "Fourier features let networks learn high frequency functions in low dimensional domains," *Advances in Neural Information Processing Systems*, vol. 33, pp. 7537–7547, 2020.
- [85] P. Bilic, P. Christ, H. B. Li, E. Vorontsov, A. Ben-Cohen, G. Kaissis, A. Szeskin, C. Jacobs, G. E. H. Mamani, G. Chartrand *et al.*, "The liver tumor segmentation benchmark (lits)," *Medical Image Analysis*, vol. 84, p. 102680, 2023.
- [86] W. Crum, O. Camara, and D. Hill, "Generalized overlap measures for evaluation and validation in medical image analysis," *IEEE Transactions on Medical Imaging*, vol. 25, no. 11, pp. 1451–1461, 2006.
- [87] D. Zhou, J. Fang, X. Song, C. Guan, J. Yin, Y. Dai, and R. Yang, "Iou loss for 2d/3d object detection," *CoRR*, vol. abs/1908.03851, 2019. [Online]. Available: <http://arxiv.org/abs/1908.03851>
- [88] M.-P. Dubuisson and A. K. Jain, "A modified hausdorff distance for object matching," in *Proceedings of 12th international conference on pattern recognition*, vol. 1. IEEE, 1994, pp. 566–568.
- [89] H.-H. Chang, A. H. Zhuang, D. J. Valentino, and W.-C. Chu, "Performance measure characterization for evaluating neuroimage segmentation algorithms," *Neuroimage*, vol. 47, no. 1, pp. 122–135, 2009.
- [90] F. P. Kuhl and C. R. Giardina, "Elliptic fourier features of a closed contour," *Computer graphics and image processing*, vol. 18, no. 3, pp. 236–258, 1982.